

UNCLASSIFIED  
~~CONFIDENTIAL~~

Copy 6  
RM A54H27

NACA RM A54H27



# RESEARCH MEMORANDUM

LONGITUDINAL AERODYNAMIC CHARACTERISTICS TO LARGE  
ANGLES OF ATTACK OF A CRUCIFORM MISSILE  
CONFIGURATION AT A MACH NUMBER OF 2

By J. Richard Spahr

Ames Aeronautical Laboratory  
Moffett Field, Calif.

CLASSIFICATION CHANGED  
To UNCLASSIFIED

By authority of *STAR* Date *3-31-71*  
*V.9, No.1* *blm*  
*8-f 71*

CLASSIFIED DOCUMENT

This material contains information affecting the National Defense of the United States within the meaning of the espionage laws, Title 18, U.S.C., Secs. 793 and 794, the transmission or revelation of which in any manner to an unauthorized person is prohibited by law.

NATIONAL ADVISORY COMMITTEE  
FOR AERONAUTICS

WASHINGTON  
December 6, 1954

~~CONFIDENTIAL~~  
UNCLASSIFIED

Y

NACA RM A54H27

UNCLASSIFIED

NASA Technical Library



3 1176 01434 7729

NATIONAL ADVISORY COMMITTEE FOR AERONAUTICS

RESEARCH MEMORANDUM

LONGITUDINAL AERODYNAMIC CHARACTERISTICS TO LARGE

ANGLES OF ATTACK OF A CRUCIFORM MISSILE

CONFIGURATION AT A MACH NUMBER OF 2 **CLASSIFICATION CHANGED**

By J. Richard Spahr

To ~~UNCLASSIFIED~~

SUMMARY

By authority of

 CSAN Date 3/31/71  
 v. 9, No. 1 Item 8/4/71

The lift, pitching-moment, and drag characteristics of a missile configuration having a body of fineness ratio 9.33 and a cruciform triangular wing and tail of aspect ratio 4 were measured at a Mach number of 1.99 and a Reynolds number of 6.0 million, based on the body length. The tests were performed through an angle-of-attack range of  $-5^\circ$  to  $28^\circ$  to investigate the effects on the aerodynamic characteristics of roll angle, wing-tail interdigitation, wing deflection, and interference among the components (body, wing, and tail). Theoretical lift and moment characteristics of the configuration and its components were calculated by the use of existing theoretical methods which have been modified for application to high angles of attack, and these characteristics are compared with experiment.

The lift and drag characteristics of all combinations of the body, wing, and tail were independent of roll angle throughout the angle-of-attack range. The pitching-moment characteristics of the body-wing and body-wing-tail combinations, however, were influenced significantly by the roll angle at large angles of attack (greater than  $10^\circ$ ). A roll from  $0^\circ$  (one pair of wing panels horizontal) to  $45^\circ$  caused a forward shift in the center of pressure which was of the same magnitude for both of these combinations, indicating that this shift originated from body-wing interference effects.

A favorable lift-interference effect (lift of the combination greater than the sum of the lifts of the components) and a rearward shift in the center of pressure from a position corresponding to that for the components occurred at small angles of attack when the body was combined with either the exposed wing or tail surfaces. These lift and center-of-pressure interference effects were gradually reduced to zero as the angle of attack was increased to large values. The effect of wing-tail interference, which influenced primarily the pitching-moment characteristics,

 UNCLASSIFIED  
 UNCLASSIFIED

is dependent on the distance between the wing trailing vortex wake and the tail surfaces and thus was a function of angle of attack, angle of roll, and wing-tail interdigitation. Although the configuration at zero roll with the wing and tail in line exhibited the least center-of-pressure travel, the configuration with the wing and tail interdigitated had the least change in wing-tail interference over the angle-of-attack range.

The lift effectiveness of the variable-incidence wing was reduced by more than 70 percent as a result of an increase in the combined angle of attack and wing incidence from  $0^\circ$  to  $40^\circ$ . The wing-tail interference (effective downwash at the tail) due to wing deflection was nearly zero as a result of a region of negative vorticity shed from the inboard portion of the wing.

The lift characteristics of the configuration and its components were satisfactorily predicted by the calculated results, but the pitching moments at large angles of attack were not because of the influence of factors for which no adequate theory is available, such as the variation of the crossflow drag coefficient along the body and the effect of the wing downwash field on the afterbody loading.

#### INTRODUCTION

The target-pursuit maneuvers or programmed trajectory of guided missiles frequently require flight at large angles of attack (of the order of  $30^\circ$ ), particularly at high altitudes. Limited experimental information at supersonic speeds indicates that the aerodynamic characteristics of missile configurations at such angles can be significantly different from those at small angles and that existing theoretical methods (based on small angle-of-attack considerations) can be inadequate for the prediction of these characteristics. These methods have been shown in references 1 and 2 to predict satisfactorily the lift and pitching-moment characteristics of a wide variety of body-wing-tail combinations at small and moderate angles of attack ( $0^\circ$  to  $20^\circ$ ), despite the neglect of the following high angle-of-attack effects:

1. Reduction in lift-curve slope of the wing with increasing angle of attack (ref. 3), an effect accounted for in the method of reference 2 by use of the experimental lift curve of the wing instead of linear theory as a basis for the calculations.
2. Effect of viscous crossflow on the wing and body loading (refs. 4 to 6).
3. Change in the wing spanwise load distribution (refs. 7 and 8) and in the character of the trailing vortex wake (ref. 9) with increasing angle of attack.

4. The destabilizing effect of roll on a cruciform wing-body combination at large angles of attack (ref. 10).

In order to obtain information on the importance of these high angle-of-attack effects, a wind-tunnel investigation was performed of the longitudinal characteristics of a representative supersonic missile configuration and various combinations of its components. The purpose of the investigation was to isolate the factors contributing to the lift, stability, and control characteristics of the complete configuration through a comparison of the experimental results with theoretical results for which as many as possible of the high angle-of-attack effects are taken into account. This investigation is part of a coordinated experimental and theoretical research program to study the aerodynamic characteristics of wings, bodies, and combinations at high angles of attack and to develop methods for predicting these characteristics. The completed portions of this research program are reported in references 4, 5, 6, 8, 9, 11, and 12.

#### NOTATION

##### Primary Symbols

All forces and moments are referred to the system of axes shown in figure 1.

$C_D$	drag coefficient, $\frac{D}{qS}$
$\Delta C_D$	rise in drag coefficient above minimum, $C_D - C_{D_{min}}$
$C_{D_{min}}$	minimum drag coefficient
$C_L$	lift coefficient, $\frac{L}{qS}$
$\Delta C_L$	change in lift coefficient due to wing deflection, $\delta$
$C_m$	pitching-moment coefficient about the 0.5l point, $\frac{\text{pitching moment}}{qSl}$ , (See fig. 2(a).)
$\Delta C_m$	change in pitching-moment coefficient due to wing deflection, $\delta$
c	local wing chord, in.
D	total drag - base drag, lb
L	lift, lb

$l$	body length, in. (See fig. 2(a).)
$q$	free-stream dynamic pressure, lb/sq in.
$s$	wing semispan, in.
$S$	body frontal area, sq in.
$x, y, z$	body axis system in which the $x$ - $z$ plane remains vertical (unrolled) as the model is rolled (See fig. 1.)
$x_1$	longitudinal axis with origin at body apex ( $x + 0.5l$ )
$\bar{x}$	longitudinal distance from moment reference point ( $0.5l$ ) to center of pressure, $-\frac{\text{pitching moment}}{\text{normal force}}$ , in.
$y_v$	lateral position of wing vortex, in.
$\alpha$	angle of attack of body, deg (See fig. 1.)
$\delta$	wing deflection about hinge line, positive when leading edge up, deg (See fig. 2(a).)
$\phi$	angle of roll in the $y$ - $z$ plane, deg (See fig. 1.)

#### Subscripts

B	body
BT	body-tail combination
BW	body-wing combination
BWT	body-wing-tail combination
opt	condition of maximum lift-drag ratio
T	exposed tail surfaces
W	exposed wing surfaces

## APPARATUS

## Wind Tunnel and Instrumentation

The Ames 1- by 3-foot supersonic wind tunnel No. 1, in which the investigation was conducted, is a closed-circuit continuous-operation wind tunnel having independently variable Mach number and Reynolds number.

The forces and moments on the model were measured by means of a three-component strain-gage balance which is illustrated in figure 3. The balance is mounted on a quadrant-type support having its center of rotation coincident with the center of the test section, thereby providing an angle-of-attack range of about  $36^\circ$  with a minimum translation of the model in the test section. The model vortex wake was observed by means of the vapor-screen flow-visualization apparatus which is described in reference 9.

## Models and Supports

The model tested in the investigation consisted of a cruciform wing-body-tail combination, the dimensional characteristics of which are presented in figure 2(a) and table I. The wing and tail panels were removable to permit testing the model as a body, body-wing combination, body-tail combination, or body-wing-tail combination. The horizontal wing panels were provided with variable incidence of  $\pm 16^\circ$ , designated wing deflection  $\delta$  throughout the report. The tail panels could be rotated about the body axis from a position in line with the wing panels to one interdigitated  $45^\circ$  and the body could be rotated  $22\text{-}1/2^\circ$ ,  $45^\circ$ , or  $90^\circ$  about its axis. The two horizontal wing panels, having variable incidence, incorporated a small gap at the body juncture. All models were constructed of steel.

The model was supported from the rear by a shrouded sting (fig. 2(b)) having its axis inclined in the vertical plane  $7^\circ$  to the balance axis for the purpose of increasing the maximum positive angle-of-attack setting from  $18^\circ$  to  $25^\circ$ .

A planar wing having the same plan form and airfoil section as the wing and tail panels on the body-wing-tail combination was provided to obtain wing alone and tail alone characteristics. This model was supported from the rear by a thin triangular vertical-fin type of support designed to minimize the effect on the wing aerodynamic forces.

## TESTS AND RESULTS

All of the tests of the investigation were performed at a Mach number of 1.99, at a Reynolds number of 6.0 million, based on the body length, and through an angle-of-attack range of approximately  $-6^\circ$  to  $28^\circ$ . Lift, drag, and pitching-moment measurements were made through this range for each of the configurations and roll angles listed in table II(a) with the horizontal wing fixed at zero incidence. These measurements were also obtained at zero roll angle for the body-wing and body-wing-tail combinations for which the wing deflection was set at angles of  $5^\circ$ ,  $8^\circ$ ,  $12^\circ$ , and  $16^\circ$ .

The results of these measurements in terms of both basic ( $C_L$ ,  $C_m$ , and  $C_D$ ) and derived ( $\bar{x}/l$ ,  $\Delta C_D/C_L^2$ , and  $L/D$ ) quantities are presented in figures 4 to 16 for the complete model and its components. The corresponding results calculated by the theoretical methods described in the Appendix are also shown on a number of these figures for purposes of direct comparison. For the complete configuration (fig. 4), two calculated pitching-moment curves are presented for each case, one extending over the lower angle-of-attack range ( $0^\circ$  to  $16^\circ$ ) and based upon the linear-theory wing spanwise load distribution, and the other one extending over the upper angle-of-attack range ( $12^\circ$  to  $28^\circ$ ) and based upon a triangular spanwise load distribution. Both the experimental and calculated results are summarized for two extreme angles of attack ( $0^\circ$  and  $26^\circ$ ) in table II.

The precision of the final results calculated from these measurements has been estimated from the square root of the sum of the squares of the uncertainty in each of the measured quantities. The following table lists the estimated error in the results, expressed in aerodynamic-coefficient form, and in the independent variables:

Quantity	Estimated error	
	$\alpha = 0^\circ$	$\alpha = 25^\circ$
$C_L$	$\pm 0.05$	$\pm 0.10$
$C_m$	$\pm 0.002$	$\pm 0.006$
$C_D$	$\pm 0.01$	$\pm 0.04$
M	$\pm 0.02$	
$\alpha$	$\pm 1.0^\circ$	
$\phi$	$\pm 2.0^\circ$	
$\delta$	$\pm 1.0$	

Vapor-screen photographs were taken of the flow at the tail-plane location for the body-wing combination at various angles of attack,

angles of roll, and wing deflections. Figure 17 presents photographs at a large angle of attack for three roll angles, and figure 18 shows photographs of the flow with the wing deflected.

## DISCUSSION

The results for the complete configuration (body-wing-tail combination) will be discussed first. In this discussion, the significant effects of the independent variables (angle of attack, angle of roll, and wing deflection) on the longitudinal characteristics will be considered, and the experimental results will be compared with the values computed by the theoretical methods described in the Appendix. The results for the configuration components (body, wing, and tail) and the body-wing and body-tail combinations will then be discussed in order to isolate the principal factors contributing to these characteristics of the complete combination and to determine the effect of the independent variables on body-wing, body-tail, and wing-tail interference.

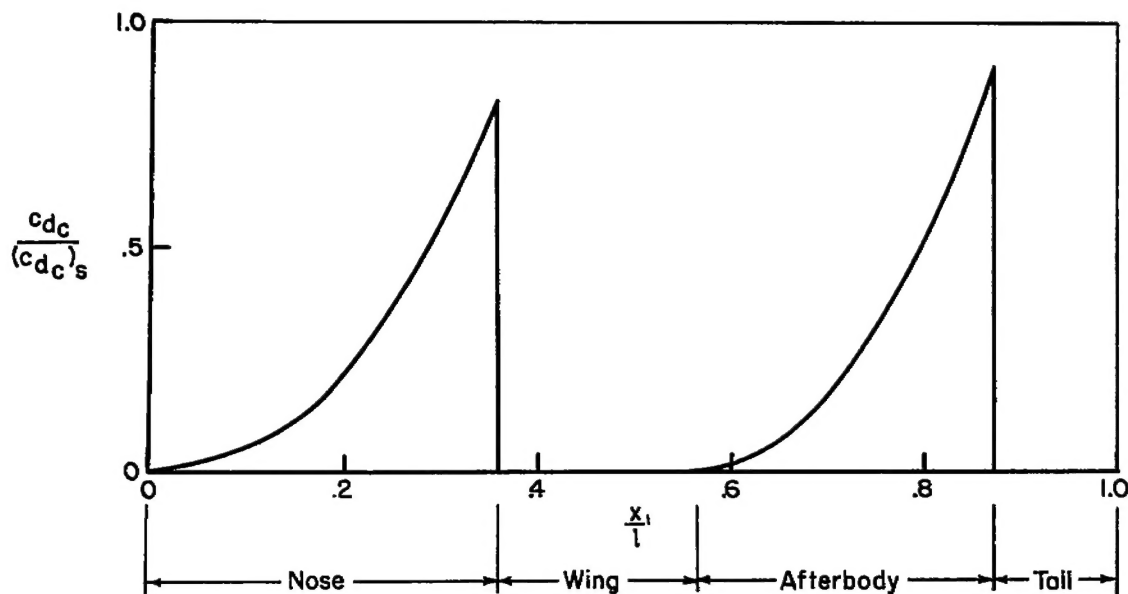
### Body-Wing-Tail Combination

Effect of roll angle.— The influence of increasing the roll angle from  $0^\circ$  (one pair of wings horizontal) on the longitudinal characteristics is shown in figure 4 and summarized in table II(a). It is observed that the lift and drag coefficients and thus the lift-drag ratio and drag-rise factor  $\Delta C_D/C_L^2$  are essentially independent of both the roll angle and rotational orientation of the tail surfaces relative to the wing surfaces. It is noteworthy that the drag-rise factor increases only slightly through the angle-of-attack range. The variation of pitching-moment coefficient  $C_m$  and center-of-pressure position  $\bar{x}$  with angle of attack  $\alpha$  are influenced significantly by both the roll angle and wing-tail orientation. At angles of attack above about  $10^\circ$  a change in the roll angle from  $0^\circ$  to  $45^\circ$  reduces the static stability in a similar manner for both wing-tail positions. At angles of attack near the maximum tested, this reduction corresponds to a forward shift in the center of pressure of about 4 percent of the body length (28 percent of the wing mean aerodynamic chord) for a change in roll angle of  $45^\circ$ , as shown in figure 4(a) and table II.

The influence of roll on the pitching-moment characteristics is believed to be caused primarily by the change in loading on the afterbody (portion of body between the wing and tail), due to the wing downwash field as the model roll angle is varied. The results of reference 10 have shown that this effect of roll on a wing-body combination is completely eliminated by the removal of the afterbody.



The calculated lift curves (fig. 4(a)) are in close agreement with the experimental curves for all roll angles and both tail positions for angles of attack up to about  $18^\circ$ . Above this angle the lift is overestimated but by less than 10 percent. This small difference is believed to be due primarily to the theoretical assumption of a constant crossflow drag coefficient along the unwinged portions of the body; whereas the experimental results of references 5, 6, and 12 have shown that the crossflow drag coefficient varies along the length of a body in a manner similar to that for a body starting impulsively from rest. From the experimental results of reference 12, the ratio of the actual crossflow drag coefficient to the assumed (steady-state) value would be expected to vary along the body in a manner similar to the distribution shown in sketch (a). The distribution along the afterbody, however, has not been



Sketch (a)

established quantitatively and is based primarily on conjecture. Thus, it was not considered justified to incorporate in the present calculations the variations shown in sketch (a). The crossflow drag coefficient along those portions of the body occupied by the wing and tail is assumed to be zero, since the normal force on the wing-body and tail-body combinations is accounted for by another method, as described in the Appendix.

In order to show the effects of some of the flow components and theoretical assumptions on the calculated lift and moment characteristics, figure 5 has been prepared. The curves designated "total" refer to the complete body-wing-tail combination and, unless otherwise specified, include the trigonometric factor  $\sin \alpha \cos \alpha$  in the calculation of the

lift of the wing and tail surfaces (see Appendix). The first of these curves (total,  $y_v/s = 0.60$ ) was used in figure 4(a) for angles of attack from  $12^\circ$  to  $28^\circ$  and the second (total,  $y_v/s = 0.74$ ) was used for angles from  $0^\circ$  to  $16^\circ$ .

Calculations have shown that the variation in the crossflow drag coefficient of sketch (a) is of the right order of magnitude to account for the difference between the experimental and calculated total lift previously discussed. Figure 5 shows that for the complete configuration, the use of the trigonometric factor reduced the difference between the experimental and calculated lift results at large angles of attack. It is also noted from figure 5 that the influence of the assumed vortex position  $y_v/s$ , which is determined by the wing spanwise load distribution, on the lift is negligible since this effect would be expected to be confined largely to the lift of the tail surfaces and thus contribute little to the total lift.

A comparison of the pitching-moment characteristics of figure 4 shows that at zero roll angle, the pitching moments are underestimated by the theoretical method throughout the angle-of-attack range for both wing-tail orientations. It is apparent that the predicted pitching moments would be more negative if the distribution of crossflow drag coefficient shown in sketch (a) were used instead of a constant value. Figure 5 shows that the contribution of the two portions of the body to the pitching moments is large. Supplementary calculations have shown that the variation in the crossflow drag coefficient of sketch (a) is of the proper magnitude to account for the discrepancies between the experimental and calculated moment results. Figure 5 also indicates that the trigonometric factor has only a small effect on the moments and that the lateral vortex spacing  $y_v/s$  affects the contribution of wing-tail interference to the pitching moments primarily at small angles of attack, as would be expected.

Wing-control characteristics.— The effects of wing deflection on the longitudinal characteristics of the body-wing-tail combination are shown in figures 6 and 7 and are summarized in table II(b). It is observed that, as in the case of the rolled model (fig. 4), the lift and drag characteristics are little affected by the wing-tail orientation (inline or interdigitated), whereas the moment characteristics are altered somewhat by a change in tail position. Figures 6(a) and 7 show that the rate of change in lift coefficient with either angle of attack or wing deflection diminishes as either of these variables increases. It is noted, for example, from table II(b) that the lift-effectiveness parameter  $\Delta C_L/\delta$  at small wing deflections ( $\delta \rightarrow 0^\circ$ ) decreases to less than half its initial value as the angle of attack is increased from  $0^\circ$  to  $26^\circ$ ; and, at a wing deflection of  $16^\circ$ ,  $\Delta C_L/\delta$  is reduced to about one third its initial value by this increase in angle of attack. Reductions in the lift would be expected, particularly at large combined wing angles ( $\alpha + \delta$ ), as previous experimental investigations (e.g., ref. 3) have shown that the lift of

wings at supersonic speeds reaches a maximum at angles near  $45^\circ$ . The curves of figures 6(a) and 7 show that the pitching moment is only slightly affected by wing deflections at zero angle of attack; whereas at positive angles of attack sizable nonlinear effects of both angle of attack and positive wing deflection are evident for both wing-tail conditions. It is also noted that the intensity of the nonlinear variation with angle of attack (fig. 6(a)) increases as the wing deflection is increased. These pitching-moment characteristics are primarily due to wing-tail interference effects since they are not present when the tail surfaces are removed, as will be discussed later. These interference effects occur only when the angle of attack and wing deflection are of the same sign since it is for this case that the wing wake passes over the tail surfaces, the condition of maximum interference. The intensity of these effects increases with wing deflection because of the increasing strength of the vorticity in the wake.

The differences between the calculated and experimental lift results (figs. 6(a) and 7) are believed to be caused primarily by the theoretical assumption of a constant crossflow drag coefficient along the body, as pointed out in the preceding section. Calculated pitching-moment results are not presented in figures 6(a) and 7 because of the change in the spanwise load distribution due to wing incidence which influences the wing-tail interference but cannot be adequately predicted by existing methods. As pointed out in reference 1, the loading near the juncture of large-aspect-ratio wings is less than the maximum loading. This apparently has a large effect on the pitching moments but only a secondary effect on the lift.

#### Body

The results for the isolated body are presented in figure 8 and summarized in table II(a). It is noted that the lift increases with angle of attack in a manner characteristic of a body of revolution having both potential and viscous-separation crossflow and that the calculated results accounting for both of these components of the flow are in close agreement with the experimental results. The pitching moments, on the other hand, are closely predicted only at angles of attack near zero, being increasingly overpredicted at larger angles. These comparisons between the calculated and experimental lift and moment results are in accord with similar comparisons of reference 5.

The drag results of figure 8(b) show a rapid decrease in the drag-rise factor at small angles of attack to an asymptotic value at large angles. It is noteworthy that the maximum lift-drag ratio occurs at large angles of attack and that the lift-drag ratio at an angle of attack of  $26^\circ$  is virtually unchanged by the addition of wing or tail surfaces (table II(a)).

## Wing and Tail

The results for the wing and for the tail are presented in figure 9 and summarized in table II(a). It is observed that the lift-curve slope decreases with increasing angle of attack, as would be expected from the fact that the maximum lift of supersonic wings occurs near  $45^\circ$  (ref. 3), and the moment varies such that the center of pressure moves slightly rearward. It is noted that the lift and moment results as calculated by the modified linear-theory method (see Appendix) are in close agreement with the experimental results. The small differences in center-of-pressure location between the calculated ( $\bar{x}/l = 0$  for the wing) and experimental results at small angles of attack are probably due to wing-profile (second-order) effects which were neglected in the theoretical method. It is noted that the center of pressure remains essentially constant throughout the entire angle-of-attack range which might be expected from the fact that both linear theory (applicable to small angles of attack) and impact theory (applicable to angles approaching  $90^\circ$ ) predict that the center of pressure of a triangular wing is located at the centroid of area.

The drag characteristics (fig 9(b)) show that the drag-rise factor  $\Delta C_D/C_L^2$  increases with angle of attack, especially at the larger angles, resulting in an increase of nearly 50 percent over the angle-of-attack range of  $0^\circ$  to  $30^\circ$ . This increase results from the decrease in lift-curve slope with increasing angle of attack. If it is assumed that the resultant-force vector acts normal to the wing, it can be shown that the drag-rise factor is inversely proportional to the factor  $\cos^2\alpha$  which accounts quantitatively for the experimental increase with angle of attack. It is noteworthy that this increase in  $\Delta C_D/C_L^2$  with angle of attack for the wing is in contrast to the decrease for the body (fig. 8(b)) as previously discussed.

## Body-Wing and Body-Tail Combinations

Effect of roll angle.— The influence of roll position on the longitudinal characteristics of the body-wing and body-tail combinations is shown in figures 10 and 11, respectively, and in table II(a). It is observed that, as is the case for the body-wing-tail combination (fig. 4), discussed previously, the lift and drag characteristics of both the body-wing and body-tail combinations are independent of the roll angle; whereas, at angles of attack greater than about  $10^\circ$ , the roll angle has a pronounced influence on the pitching-moment characteristics of the body-wing combination. A similar effect of roll on pitching moment at large angles of attack is also shown by unpublished data for a cruciform-wing and body combination. The results for the cruciform wing alone, however, showed no such effect, indicating that the source of this roll

effect lies in the interference fields between the wing and body. These data and the results of reference 10 have shown conclusively that the effect of roll on pitching moment is due to the change in loading on the afterbody. It is noteworthy that the center-of-pressure shift due to roll for the body-wing combination is in the same direction and is of the same order of magnitude as that previously discussed for the body-wing-tail combination. The center-of-pressure travel due to angle of attack is noted to be the least for a roll angle of  $45^\circ$  in contrast to the corresponding center-of-pressure travel for the body-wing-tail combination (fig. 4(a)) which is the greatest for this roll angle.

Figure 11(a) shows that in contrast to the characteristics of the body-wing combination, the pitching moment and center-of-pressure position for the body-tail combination are independent of roll angle throughout the angle-of-attack range. The difference between these two combinations in this respect follows from the fact that the body-tail combination essentially has no afterbody, and thus the source of the effect of roll on the pitching moments is not present.

The lift curves of both combinations (figs. 10(a) and 11(a)) calculated by the modified linear theory described in the Appendix are in close agreement with the experimental curves for all roll angles at angles of attack up to about  $18^\circ$ , above which the results are overestimated but by less than 10 percent. This comparison is in agreement with that for the body-wing-tail combination, indicating that the source of the difference between the calculated and experimental results lies in the assumption of a constant crossflow drag coefficient along the body, as discussed for the body-wing-tail combination. The calculated and experimental results for pitching moment, and thus for center-of-pressure position, for the body-wing combination (fig. 10(a)) are in close agreement at angles of attack up to about  $12^\circ$  above which significant differences are present, particularly at a roll angle of  $0^\circ$ . Figure 11(a) shows that the experimental and calculated pitching-moment results for the body-tail combination are in close agreement throughout the angle-of-attack range.

The drag results of figures 10(b) and 11(b) show that the drag-rise factor  $\Delta C_D/C_L^2$  of the body-wing combination increases with angle of attack but by a much smaller percentage than that for the isolated wing (fig. 9(b)), indicating the influence of the body. The drag-rise factor for the body-tail combination, however, is noted to decrease with angle of attack, reflecting the predominant influence of the body (see fig. 8(b)). The maximum lift-drag ratio for the body-wing combination is considerably greater than that for the body-tail combination (see table II(a)), as would be expected, but at angles of attack near the maximum tested, the lift-drag ratios of both combinations are essentially the same as that for the isolated body.

Wing-control characteristics.- The effects of wing deflection on the longitudinal characteristics of the body-wing combination are shown in figures 12 and 13 and summarized in table II(b). These effects on the lift characteristics are very similar to those for the body-wing-tail combination (figs. 6(a) and 7) wherein the rate of change in lift coefficient with either angle of attack or wing deflection diminishes as either of these variables increases. The pitching-moment curves (figs. 12(a) and 13) show only a relatively small influence of wing deflection, indicating that the center of pressure of the additional loading due to wing deflection is close to the moment reference point (midlength point of body) and that this loading location remains nearly constant throughout the angle-of-attack range.

A comparison of the calculated and experimental lift results of figures 12(a) and 13 shows close agreement at small angles of attack and wing deflections, but at moderate and large angles the estimates are high. At the largest angles of attack, however, the incremental lift due to wing deflection (fig. 13) is closely predicted. These differences between the calculated and experimental lift results are similar to those discussed previously for the body-wing-tail combination. The calculated and experimental pitching-moment results (figs. 12(a) and 13) are in reasonably close agreement throughout the wing-deflection range for angles of attack up to about  $14^\circ$ , above which the moments are overestimated. These differences at large angles are believed to be due primarily to the simplifying assumption used in calculating the load distribution on the body due to viscous crossflow.

### Body-Wing-Tail Interference

Body-wing and body-tail interference.- The contribution of the interactions between the pressure fields of the wing or tail surfaces and the body to the total aerodynamic forces experienced by a body-wing or body-tail combination can be determined from the forces on the isolated components and on the combination. Figures 14 and 15 present the variation of lift and center-of-pressure interference parameters with angle of attack for the body-wing and body-tail combinations, respectively. The lift-interference parameter represents the percent increase in lift of the combination over the sum of the lifts of the isolated body and exposed wing or tail panels joined together, and the center-of-pressure interference factor represents the rearward shift in center of pressure caused by combining the body and wing or tail. It is observed that a large favorable effect of interference on the lift of the body-wing or body-tail combination is present at small angles of attack, which is in agreement with the results of reference 13, but that as the angle of attack is increased, this interference effect approaches or reaches zero. Similarly, it is noted that the difference in center-of-pressure position due to interference at small angles of attack is reduced to nearly zero

as the angle of attack is increased to larger values. It thus appears that at large angles of attack, the lift or center-of-pressure location of a wing-body or tail-body combination may be estimated fairly well if the components are assumed to act separately. A comparison of the experimental interference results with those calculated by the methods of the present investigation shows that the trend of these interference factors with angle of attack is correctly predicted, and thus it appears that these methods provide a useful means of estimating the lift and moment interference characteristics of a wing- or tail-body combination at large angles of attack.

On the basis of an examination and comparison of the variation of lift with angle of attack for the combinations and isolated components, it is believed that the reduction in the favorable lift interference between the wing or tail and body with increasing angle of attack (figs. 14 and 15) is caused primarily by two effects: (1) a decrease in the favorable interference effect of the body on the exposed wing or tail and (2) the elimination or reduction of the viscous cross force on portions of the body due to addition of the wing or tail surfaces. The first effect arises from the fact that the wing in the presence of the body is operating at a larger effective angle of attack (due to the forebody upwash field) than is the isolated wing at the same geometric angle of attack, and that the lift effectiveness  $CL/\alpha$  of the wing or tail (fig. 9(a)) decreases with angle of attack. Therefore, the ratio of the lift-curve slope of the wing or tail in the presence of the body to that of the isolated wing or tail decreases with increasing angle of attack. The second effect consists of the elimination of the viscous cross force on the portions of the body to which the wing or tail surfaces are added and also the reduction in the cross force on the afterbody due to the wing downwash field. This effect causes a decrease in the lift interference with increasing angle of attack because of the fact that the viscous cross force is approximately proportional to the square of the angle of attack, whereas the cross force of the winged portion of the body is directly proportional to the angle. It is estimated that the lift-interference characteristics of the body-wing combination (fig. 14) are caused by both of these effects; whereas those of the body-tail combination (fig. 15) are caused primarily by the first effect, as the influence of the body upwash field on the tail surfaces is large and the crossflow blanketed area is small. The reduction in the difference between the center of pressure of the body and wing or body and tail in combination and that of the components acting separately as the angle of attack is increased (figs. 14 and 15) is also the result of these two effects just discussed. It is estimated that the second effect predominates for the body-wing combination, as the wing center of pressure is assumed to be unaffected by the forebody upwash field in the calculated results. For the body-tail combination, both effects are important.

Wing-tail interference.- An estimation of the contribution of the interference between the wing induced flow and the tail surfaces in the



presence of an intervening body to the total aerodynamic forces and moments of a body-wing-tail combination can be obtained from the pitching-moment characteristics of the body alone and in various combinations with the wings and tail surfaces. Such a wing-tail interference factor is presented in figure 16 for both wing-tail orientations as a function of angle of attack. This factor, which is the ratio of the contribution of the tail surfaces to the pitching moment with the wings present to the contribution with the wings removed, represents primarily the effective-downwash parameter  $1 - \frac{\epsilon}{\alpha}$ , where  $\epsilon$  is an average downwash angle of the flow at the tail surfaces due to the wing. A value of zero for the interference factor corresponds to a complete cancellation of the tail load by the wing wake ( $\epsilon = \alpha$ ) and a value of one corresponds to no wing-tail interference ( $\epsilon = 0$ ). The variations shown in figure 16 can be explained on a qualitative basis by a consideration of the distance of the wing trailing vortex wake normal to the tail surfaces. From vapor-screen photographs similar to those presented in figure 17, the measurements of these distances have been made, and it was found that the vortex wake from each wing trails downstream in approximately a horizontal streamwise plane. It is expected that the downwash at the tail and thus the wing-tail interference would be large at angles of attack where the wing wake is close to the tail surfaces and smaller at angles where the wake is farther away. Thus, for the inline configuration the interference is large at small angles of attack since the trailing vortex wake from each wing panel is close to the corresponding tail surface for any angle of roll. For a roll angle of  $0^\circ$  the interference decreases with increasing angle of attack as the wing wake becomes progressively farther away from the tail surfaces. For a roll angle of  $45^\circ$ , it is noted that the interference decreases as the angle is increased to about  $16^\circ$ , above which the interference increases. This latter effect is due to the influence of the vortex wake from the lower wing panels on the lift of the upper tail panels. With the wing and tail interdigitated, an increase in the wing-tail interference is noted in the angle-of-attack range of about  $6^\circ$  to  $16^\circ$ , especially for the rolled case. This effect is caused by the passage of the vortex wake from one pair of wing panels over one pair of tail surfaces in this region for both roll angles.

Figure 16 shows that the trend in the wing-tail interference factor with angle of attack is approximately predicted by the calculated results but that the magnitude of this factor is underestimated in most cases, particularly for the unrolled configuration. These differences are caused by the approximations and simplifying assumptions in the theoretical method which have been previously discussed in relation to the characteristics of the body-wing-tail combination.



## CONCLUSIONS

The longitudinal aerodynamic characteristics (lift, pitching moment, and drag) of a missile configuration having a cruciform triangular wing and tail of aspect ratio 4 were investigated experimentally at a Mach number of 1.99 over a wide angle-of-attack range to determine the effects of roll angle, wing-tail interdigitation, wing deflection, and interference among the components. The experimental results for the components and combinations were compared with values calculated from available theoretical methods modified to account for high angle-of-attack effects. On the basis of this investigation, the following principal conclusions have been drawn:

1. The lift and drag characteristics of the configuration and its components were independent of roll angle and of wing-tail orientation, and the lift characteristics over the angle-of-attack range were satisfactorily predicted by a modified linear theory.

2. At large angles of attack (above  $10^\circ$ ), an angle of roll caused a forward shift in the center of pressure which was of the same magnitude for the body-wing and body-wing-tail combinations. This effect, which is believed to be caused by the influence of the wing downwash field on the afterbody loading, cannot be treated adequately by existing theory, and further research is needed before the pitching-moment characteristics can be predicted at high angles of attack.

3. The favorable lift-interference effect and the rearward shift in center of pressure due to combining the body with either the exposed wing or tail surfaces were reduced to essentially zero at zero roll as the angle of attack was increased from zero to large values. Thus, at large angles of attack, the lift of a combination is equal to the sum of the lifts on its components and the center of pressure is located at the position for the components acting separately.

4. The effect of wing-tail interference, which influenced primarily the pitching-moment characteristics, is dependent on the distance between the wing trailing vortex wake and the tail surfaces and thus was a function of angle of attack, angle of roll, and wing-tail interdigitation. Although the inline configuration at zero roll exhibited the least center-of-pressure travel, the interdigitated configuration had the least change in wing-tail interference over the angle-of-attack range.

5. The lift effectiveness of the variable-incidence wing  $\Delta C_L/\delta$  was reduced by more than 70 percent due to an increase in the combined angle of attack and wing incidence from  $0^\circ$  to  $40^\circ$ . Wing-tail interference was essentially independent of wing incidence apparently as a result of low loading on the wing near the body.

Ames Aeronautical Laboratory  
National Advisory Committee for Aeronautics  
Moffett Field, Calif., Aug. 27, 1954

## APPENDIX

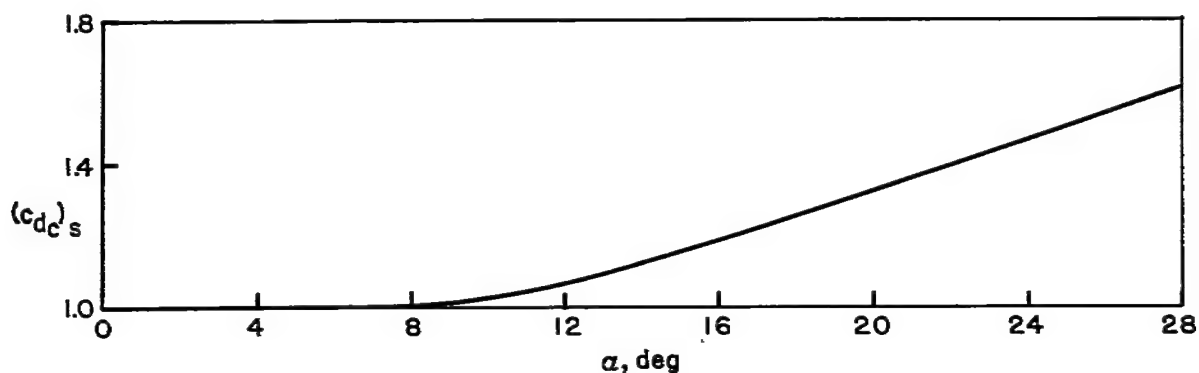
## THEORETICAL METHODS

The application and extension of existing theories used to predict the experimental lift and moment results for the configuration and its components, the assumptions and limitations of these methods, and the need for further theoretical development are described in the following paragraphs. The methods used for the isolated components are considered first, as they serve as a basis for those used for the combinations.

## Body

The method used for predicting the lift and moment characteristics of the isolated body follows that developed in reference 4 wherein the local cross force was considered to be composed of the sum of the force due to potential crossflow and that due to viscous crossflow. The potential cross force was calculated by means of linear theory (ref. 14) instead of slender-body theory, as used in reference 4, because the nose portion of the body was not slender. The viscous cross force was calculated from the relationship given in reference 4 in which the crossflow drag coefficient is assumed to be constant along the length of the body for a given angle of attack. In references 5, 6, and 12 this assumption is shown to be inaccurate, as it is demonstrated that the development of crossflow along a body is similar to that for a circular cylinder impulsively started from rest. As a result of assuming a constant drag along the body, the predicted center-of-pressure location was found to be forward of the experimental location. However, no analytical method has been firmly established for predicting the variation in crossflow drag coefficient along a body, and thus a constant value was used in the present calculations. The variation in this drag coefficient (based on the normal component of the dynamic pressure and on the body diameter) with angle of

attack, which is due to crossflow Mach number effects, used in the present calculations was obtained from experimental measurements for bodies and two-dimensional cylinders and is presented in sketch (b).



Sketch (b)

#### Wing and Tail

The variations of lift and moment of the wing and tail with angle of attack were calculated from the results of linearized wing theory modified as follows so as to be consistent with certain high angle-of-attack characteristics. The linearized supersonic wing theory, which is based on assumptions satisfied only at small angles of attack, gives the result that the lift coefficient of a thin wing is directly proportional to the angle of attack; that is,

$$C_L = C_{L\alpha} \alpha \quad (A1)$$

where  $C_{L\alpha}$  is a function of only the plan form and the Mach number. This result has been used extensively in the successful prediction of the lift of wings at small and moderate angles of attack; at larger angles the lift is overestimated. The experimental results of reference 3 show that the lift coefficient reaches a maximum value at angles of attack near  $45^\circ$ , and it is obvious that the lift would decline to zero as the angle is further increased to  $90^\circ$ . Thus it appears that a relationship satisfying these characteristics at high angles of attack and also equation (A1) at small angles might prove useful in predicting the lift of wings up to angles of attack beyond the linear range. Such a relationship is obtained by a simple trigonometric modification of equation (A1) to

$$C_L = C_{L\alpha} \sin \alpha \cos \alpha \quad (A2)$$

For the wing and tail of the present investigation,

$$C_{L\alpha} = \frac{4}{\sqrt{M^2-1}} = 2.33 \text{ per radian}$$

(ref. 15), and thus the lift coefficient of the wing and tail based on its plan-form area is given by the expression

$$C_L = 2.33 \sin \alpha \cos \alpha \quad (A3)$$

The center of pressure is located at the centroid of area at small angles of attack, according to linear theory and also at an angle of attack of  $90^\circ$ , according to impact theory. Thus, it is assumed that the center of pressure remains at this location throughout the angle-of-attack range. The resulting expression for the pitching-moment coefficient then is given by the expression

$$C_m = -2.33 \frac{\bar{x}}{l} \sin \alpha \quad (A4)$$

since the pitching moment is equal to the product of the center-of-pressure position  $\bar{x}$  and the normal force.

#### Body-Wing and Body-Tail Combinations

The lift and pitching moments on the body-wing and body-tail combinations were taken as the algebraic sum of those on the forebody, on the wing and winged portion of the body, and on the afterbody (behind the wing). The lift and moment on the forebody were calculated by the method described previously for the isolated body. The characteristics for the winged portion of the body were computed essentially by the results developed in reference 13 and extended to variable wing incidence in references 16 and 17. These results were modified to include the high angle-of-attack relationships for the wing and tail surfaces described previously. The resulting relationships for the lift and moment on the winged portion of the body are

$$C_L = \frac{k_1 \alpha + k_2 \delta}{\alpha + \delta} C_{L\alpha_W} \sin(\alpha + \delta) \cos(\alpha + \delta) \quad (A5)$$

$$C_m = \frac{k_3 \alpha + k_4 \delta}{\alpha + \delta} C_{L\alpha_W} \sin(\alpha + \delta) \quad (A6)$$

where

$$k_1 = K_W(B) + K_B(W)$$

$$k_2 = k_W(B) + k_B(W)$$

$$k_3 = K_W(B) \frac{l_M - l_{W(B)}}{l_R} + K_B(W) \frac{l_M - l_{B(W)}}{l_R}$$

$$k_4 = k_W(B) \frac{l_M - l_{W(B)}}{l_R} + k_B(W) \frac{l_M - l_{B(W)}}{l_R}$$

and the  $K$  and  $k$  factors are the interference factors due to angle of attack  $\alpha$  and wing deflection  $\delta$ , respectively, and the  $l$  quantities are the longitudinal distances used in reference 1.

The lift and moment characteristics contributed by the afterbody of the body-wing combination were calculated from the loading due to the net crossflow as influenced by the wing downwash field. This loading on the afterbody is given by the expression

$$\frac{dC_L}{dx} = 2 \frac{d}{dx} (\alpha - \epsilon) + \frac{2r}{S} c_{dc} (\alpha - \epsilon)^2 \quad (A7)$$

where the first term represents the potential cross force according to slender-body theory and the second term represents the viscous cross force according to reference 4 and where  $\epsilon$  is the downwash angle at the location of the body axis,  $r$  is the body radius, and  $c_{dc}$  is the crossflow drag coefficient. The trailing vortex wake from each wing panel was replaced by a single line vortex trailing streamwise from which the downwash angle was determined. The crossflow drag coefficient was taken from the curve shown in sketch (b) (p. 19) as a function of the effective angle of attack  $\alpha - \epsilon$  instead of the body angle of attack  $\alpha$ .

#### Body-Wing-Tail Combination

The lift and moment characteristics of the complete configuration were calculated in the same manner as those for the combinations just described, with the addition of the effects of wing-tail interference. The method used in determining these interference effects follows that presented in reference 1 wherein the trailing vortex wake from each wing panel is replaced by a single line vortex trailing streamwise and the resulting influence on the lift of each tail surface is evaluated. For the lower angle-of-attack range ( $0^\circ$  to  $16^\circ$ ), these vortices were assumed to originate at the spanwise location given by linear wing theory and,

for the higher range ( $12^\circ$  to  $28^\circ$ ), the vortices were assumed to originate at the midspan position of the exposed-wing-panel trailing edge. Actually, of course, a gradual change from the low angle-of-attack lateral vortex position to the high angle position would be expected to take place, but no method is available for the prediction of this change with angle of attack. Certain adaptations and assumptions were required, however, in applying the method to wing and tail roll angles of other than  $0^\circ$ . It was assumed that for the model at a roll angle of  $45^\circ$  the line vortices from all four wing surfaces were of equal strength, a result predicted by linear theory for cruciform wings.

## REFERENCES

1. Nielsen, Jack N., Kaattari, George E., and Anastasio, Robert F.: A Method for Calculating the Lift and Center of Pressure of Wing-Body-Tail Combinations at Subsonic, Transonic, and Supersonic Speeds. NACA RM A53G08, 1953.
2. Edwards, S. Sherman: Experimental and Theoretical Study of Factors Influencing the Longitudinal Stability of an Air-to-Air Missile at a Mach Number of 1.4. NACA RM A51J19, 1952.
3. Gallagher, James J., and Mueller, James N.: Preliminary Tests to Determine the Maximum Lift of Wings at Supersonic Speeds. NACA RM L7J10, 1947.
4. Allen, H. Julian: Estimation of the Forces and Moments Acting on Inclined Bodies of Revolution of High Fineness Ratio. NACA RM A9I26, 1949.
5. Allen, H. Julian, and Perkins, Edward W.: Characteristics of Flow Over Inclined Bodies of Revolution. NACA RM A50L07, 1951.
6. Perkins, Edward W., and Kuehn, Donald M.: Comparison of the Experimental and Theoretical Distributions of Lift on a Slender Inclined Body of Revolution at  $M = 2$ . NACA RM A53E01, 1953.
7. Hatch, John E., and Hargrave, L. Keith: Effect of Reynolds Number on the Aerodynamic Characteristics of a Delta Wing at Mach Number of 2.41. NACA RM L51H06, 1951.
8. Kaattari, George E.: Pressure Distribution on Triangular and Rectangular Wings to High Angles of Attack. Mach Numbers 1.45 and 1.97. NACA RM A54D19, 1954.
9. Spahr, J. Richard, and Dickey, Robert R.: Wind-Tunnel Investigation of the Vortex Wake and Downwash Field Behind Triangular Wings and Wing-Body Combinations at Supersonic Speeds. NACA RM A53D10, 1953.
10. Krenkel, A. R.: GMS Interim Report on Wing-Body Interference Phenomena. Rep. 3524, McDonnell Aircraft Corp., St. Louis, Mo., 1954.
11. Gowen, Forrest E.: Buffeting of a Vertical Tail on an Inclined Body at Supersonic Mach Numbers. NACA RM A53A09, 1953.
12. Perkins, Edward W., and Jorgensen, Leland H.: Comparison of Experimental and Theoretical Normal-Force Distributions (Including Reynolds Number Effects) on an Ogive-Cylinder Body at Mach Number 1.98. NACA RM A54H23, 1954.



13. Nielsen, Jack N., Katzen, Elliott D., and Tang, Kenneth K.: Lift and Pitching-Moment Interference Between a Pointed Cylindrical Body and Triangular Wings of Various Aspect Ratios at Mach numbers of 1.50 and 2.02. NACA RM A50F06, 1950.
14. Tsien, Hsue-Shen: Supersonic Flow Over an Inclined Body of Revolution. Jour. Aero. Sci., vol. 5, no. 12, Oct. 1938, pp. 480-483.
15. Puckett, Allen E.: Supersonic Wave Drag of Thin Airfoils. Jour. Aero. Sci., vol. 13, no. 9, Sept. 1946, pp. 475-484.
16. Nielsen, Jack N., and Kaattari, George E.: Method for Estimating Lift Interference of Wing-Body Combinations at Supersonic Speeds. NACA RM A51J04, 1951.
17. Kaattari, George E., Nielsen, Jack N., and Pitts, William C.: Method for Estimating Pitching-Moment Interference of Wing-Body Combinations at Supersonic Speeds. NACA RM A52B06, 1952.

TABLE I.- GEOMETRIC CHARACTERISTICS OF MODEL

Body	
Fineness ratio . . . . .	9.33
Frontal area, sq in. . . . .	0.995
Transverse (plan-form) area, sq in. . . . .	10.47
Volume, cu in. . . . .	8.83
Exposed wing panels	
Plan-form area (per pair), sq in. . . . .	5.06
Mean aerodynamic chord, in. . . . .	1.50
Aspect ratio . . . . .	4
Maximum thickness . . . . .	0.08c
Position of maximum thickness . . . . .	0.5c
Exposed tail panels	
Plan-form area (per pair), sq in. . . . .	1.56
Mean aerodynamic chord, in. . . . .	0.833
Aspect ratio . . . . .	4
Maximum thickness . . . . .	0.08c
Position of maximum thickness . . . . .	0.5c

NACA

TABLE II.- SUMMARY OF RESULTS

(a) Characteristics with fixed controls,  $\delta = 0^\circ$ 

Config- uration (1)	$\phi$ , deg	$\frac{C_L}{\alpha}$		$\frac{C_m}{\alpha}$		$\bar{X}$ $\bar{I}$		$\frac{L}{D}$		$\alpha_{opt}$ , deg
		$\alpha \rightarrow 0^\circ$ per deg	$\alpha = 26^\circ$ per deg	$\alpha \rightarrow 0^\circ$ per deg	$\alpha = 26^\circ$ per deg	$\alpha \rightarrow 0^\circ$	$\alpha = 26^\circ$	Maximum $\alpha = \alpha_{opt}$	$\alpha = 26^\circ$	
B	0	0.046 (.043)	0.137 (.145)	0.0150 (.0155)	0.0023 (.0084)	-0.33 (-.36)	-0.018 (-.054)	2.55 ---	1.82 ---	14.3 ---
$W_H$	0	.221 (.208)	.173 (.160)	.0015 (0)	.0006 (0)	-.007 (0)	-.004 (0)	5.50 ---	1.95 ---	5.2 ---
$T_H$	0	.0683 (.0640)	.0538 (.0560)	-.0306 (-.0288)	-.0272 (-.0279)	.447 (.451)	.450 (.451)	5.50 ---	1.95 ---	5.2 ---
BT	0	.135 (.131)	.189 (.205)	-.0273 (-.0239)	-.0223 (-.0220)	.202 (.183)	.104 (.097)	2.90 ---	1.82 ---	10.4 ---
	22.5	.135 (.131)	.189 (.205)	-.0273 (-.0239)	-.0234 (-.0220)	.202 (.183)	.109 (.097)	2.90 ---	1.82 ---	10.4 ---
	45	.135 (.131)	.189 (.205)	-.0273 (-.0239)	-.0236 (-.0220)	.202 (.183)	.110 (.097)	2.90 ---	1.82 ---	10.4 ---
BW	0	.347 (.334)	.326 (.348)	.0104 (.0110)	.0047 (.0104)	-.0298 (-.0329)	-.003 (-.026)	3.51 ---	1.83 ---	7.6 ---
	22.5	.347 (.334)	.326 (.347)	.0104 (.0110)	.0011 (.0107)	-.0298 (-.0329)	-.012 (-.026)	3.51 ---	1.83 ---	7.6 ---
	45	.347 (.334)	.326 (.346)	.0104 (.0110)	.0110 (.0110)	-.0298 (-.0329)	-.030 (-.027)	3.51 ---	1.83 ---	7.6 ---
BWT <sup>+</sup>	0	.413 (.382)	.367 (.396)	-.0205 (-.0103)	-.0235 (-.0148)	.0497 (.0269)	.056 (.034)	3.51 ---	1.80 ---	7.6 ---
	22.5	.415 (.394)	.365 (.398)	-.0187 (-.0155)	-.0178 (-.0115)	.0450 (.0395)	.041 (.026)	3.51 ---	1.80 ---	7.6 ---
	45	.417 (.394)	.358 (.398)	-.0180 (-.0155)	-.0078 (-.0115)	.0432 (.0395)	.020 (.026)	3.51 ---	1.80 ---	7.6 ---
BWT <sup>x</sup>	0	.425 (.394)	.361 (.390)	-.0280 (-.0155)	-.0221 (-.0110)	.0659 (.0395)	.054 (.026)	3.54 ---	1.81 ---	7.6 ---
	22.5	.430 (.402)	.358 (.388)	-.0270 (-.0194)	-.0136 (-.0119)	.0628 (.0482)	.034 (.028)	3.54 ---	1.81 ---	7.6 ---
	45	.437 (.402)	.350 (.388)	-.0260 (-.0194)	-.0060 (-.0119)	.0595 (.0482)	.015 (.028)	3.54 ---	1.81 ---	7.6 ---

(b) Control characteristics,  $\phi = 0^\circ$ 

Config- uration (1)	$\frac{\Delta C_L}{\delta}$				$\frac{\Delta C_m}{\delta}$			
	$\delta \rightarrow 0^\circ$		$\delta = 16^\circ$		$\delta \rightarrow 0^\circ$		$\delta = 16^\circ$	
	$\alpha = 0^\circ$ per deg	$\alpha = 26^\circ$ per deg	$\alpha = 0^\circ$ per deg	$\alpha = 26^\circ$ per deg	$\alpha = 0^\circ$ per deg	$\alpha = 26^\circ$ per deg	$\alpha = 0^\circ$ per deg	$\alpha = 26^\circ$ per deg
$W_H$	0.221 (.208)	0.100 (.128)	0.198 (.197)	--- (0.075)	0.0015 (0)	0 (0)	0.0005 (0)	--- (0)
BW	.218 (.238)	.092 (.059)	.195 (.223)	.059 (.043)	-.0043 (-.0026)	0 (.0105)	-.0030 (-.0014)	0 (.0066)
BWT <sup>+</sup>	.200 (.207)	.095 (.075)	.184 (.163)	.064 (.044)	0 ---	.0015 ---	0 ---	.0050 ---
BWT <sup>x</sup>	.200 (.216)	.095 (.070)	.190 (.199)	.058 (.044)	-.0030 ---	.0010 ---	-.0028 ---	.0025 ---

<sup>1</sup>Configuration designations:

B Body  
 $W_H$  Horizontal wing (exposed surfaces joined together)  
 $T_H$  Horizontal tail (exposed surfaces joined together)  
 BT Body-tail combination  
 BW Body-wing combination  
 BWT<sup>+</sup> Body-wing-tail combination with wing and tail in line  
 BWT<sup>x</sup> Body-wing-tail combination with wing and tail interdigitated

Note: The values presented within parentheses are calculated results corresponding to the experimental results directly above.

NACA

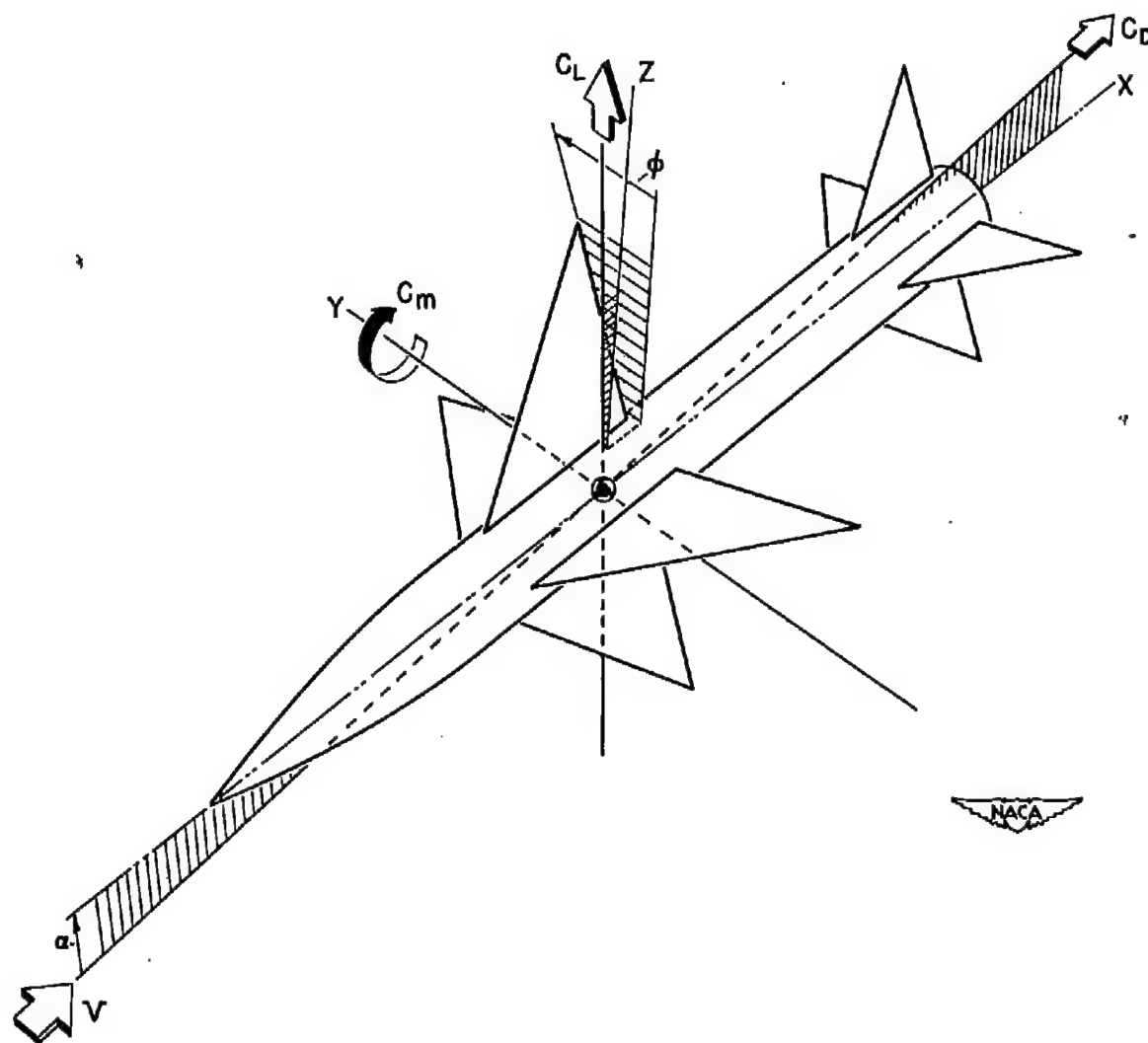
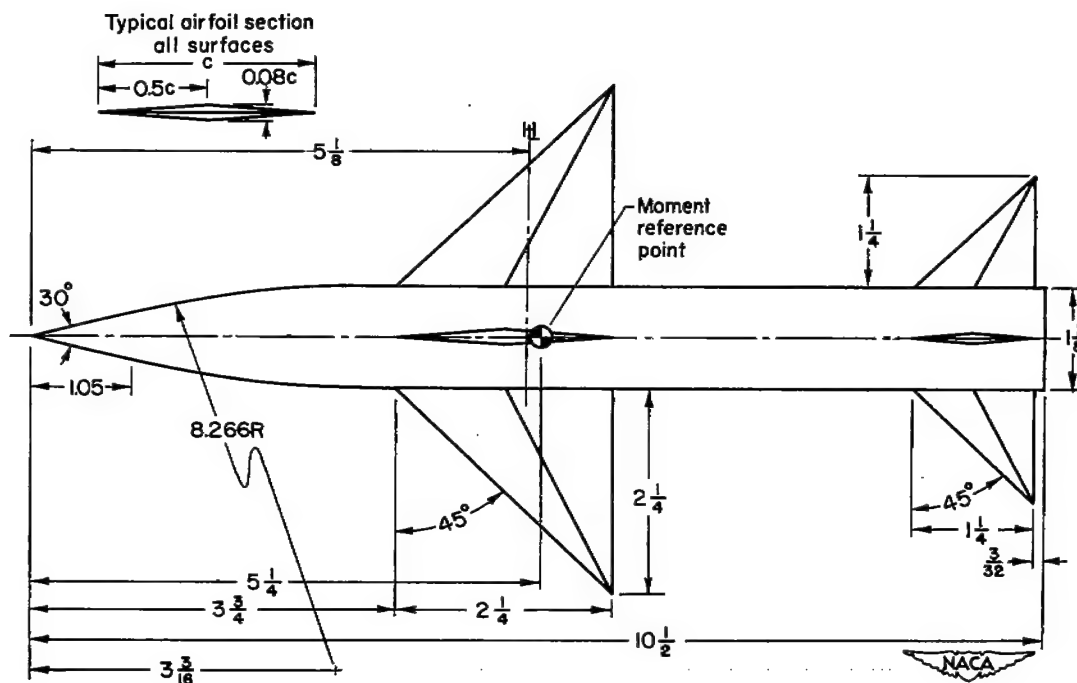
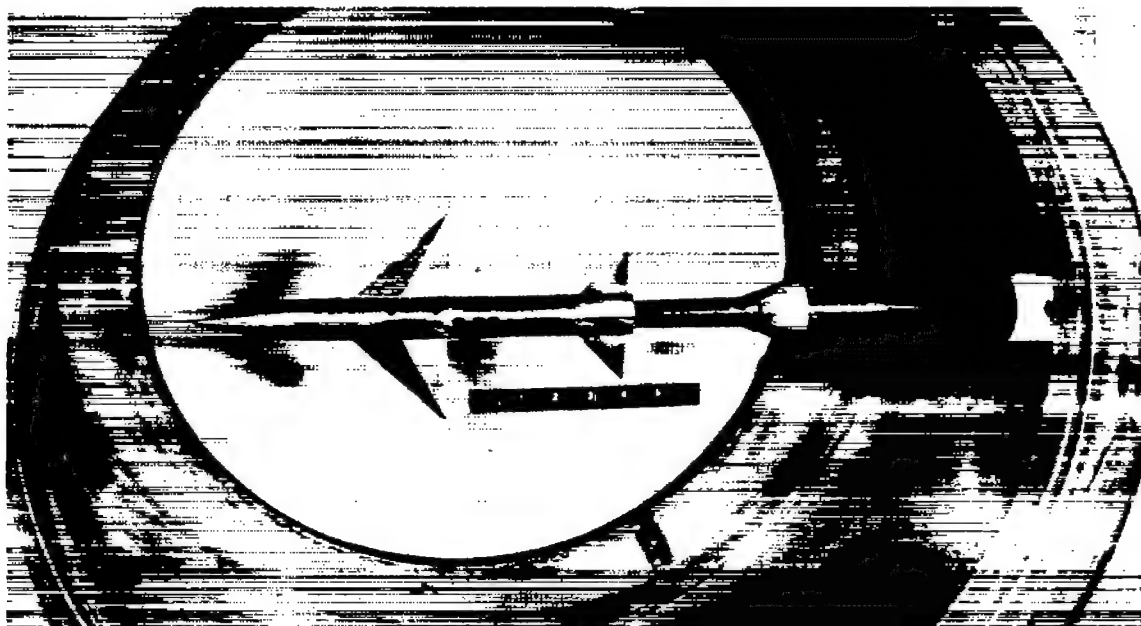


Figure 1.- Coordinate system and sign convention.



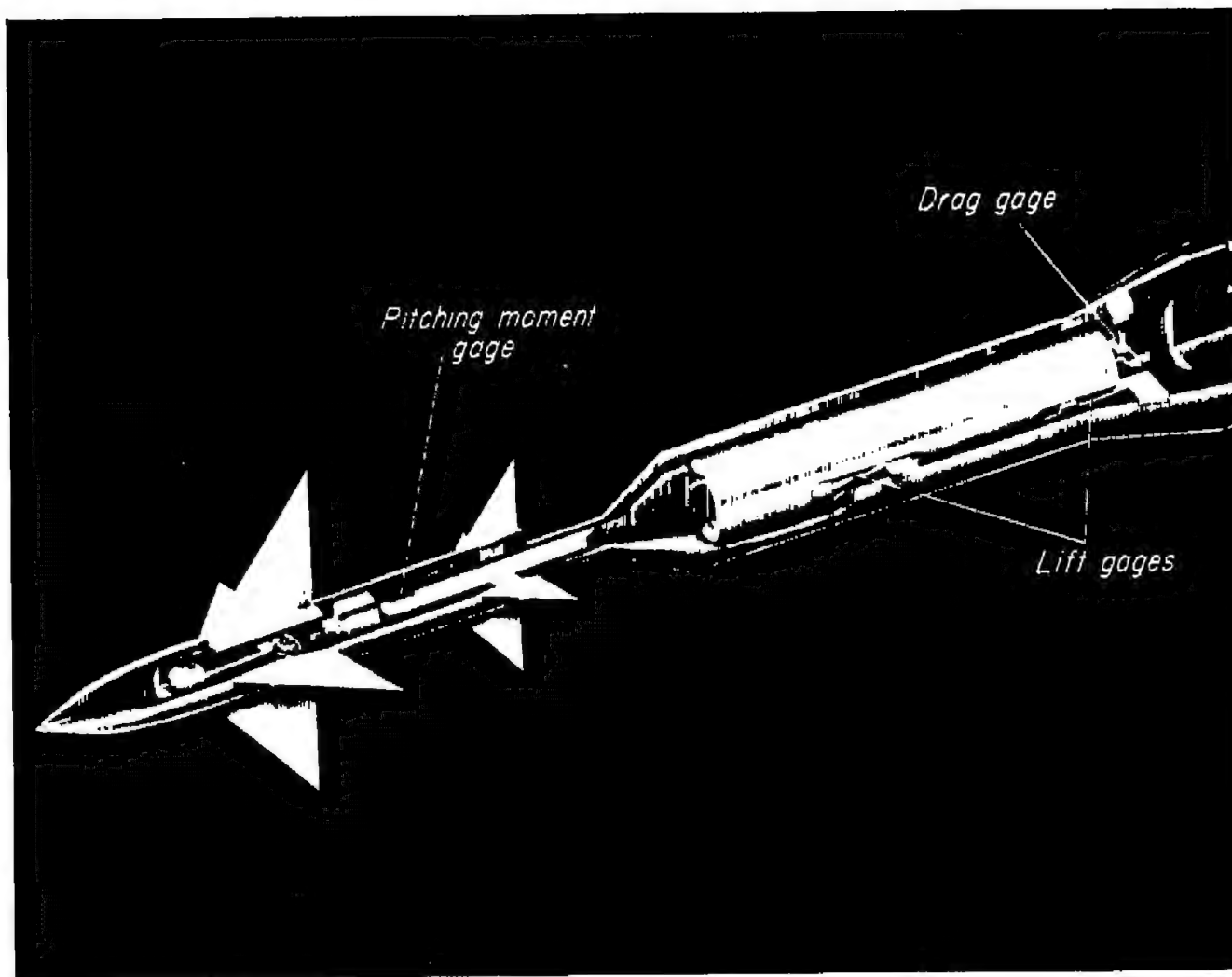
(a) Model geometry. All dimensions in inches.



A-15386

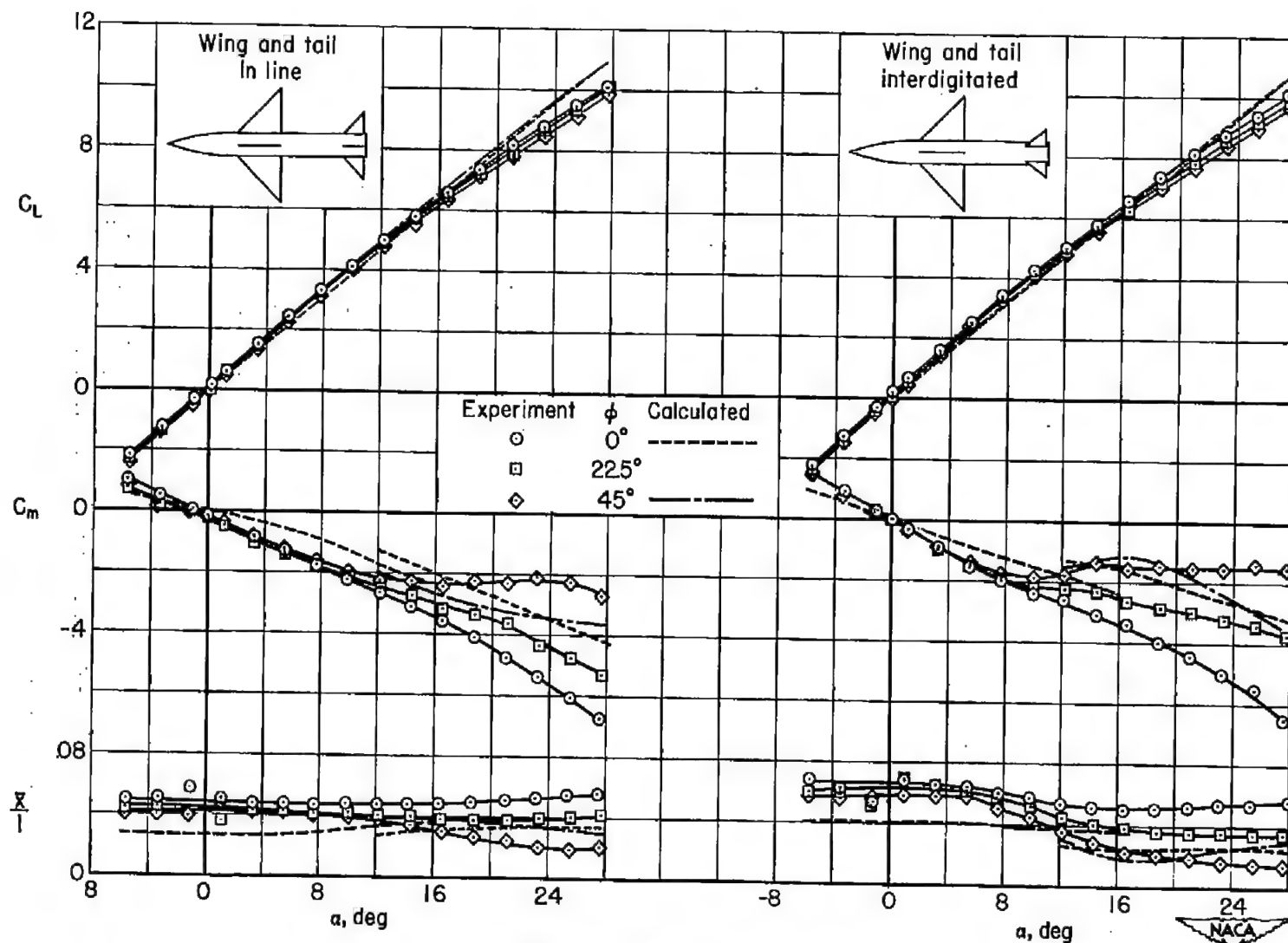
(b) View of model in wind tunnel.

Figure 2.- Model.



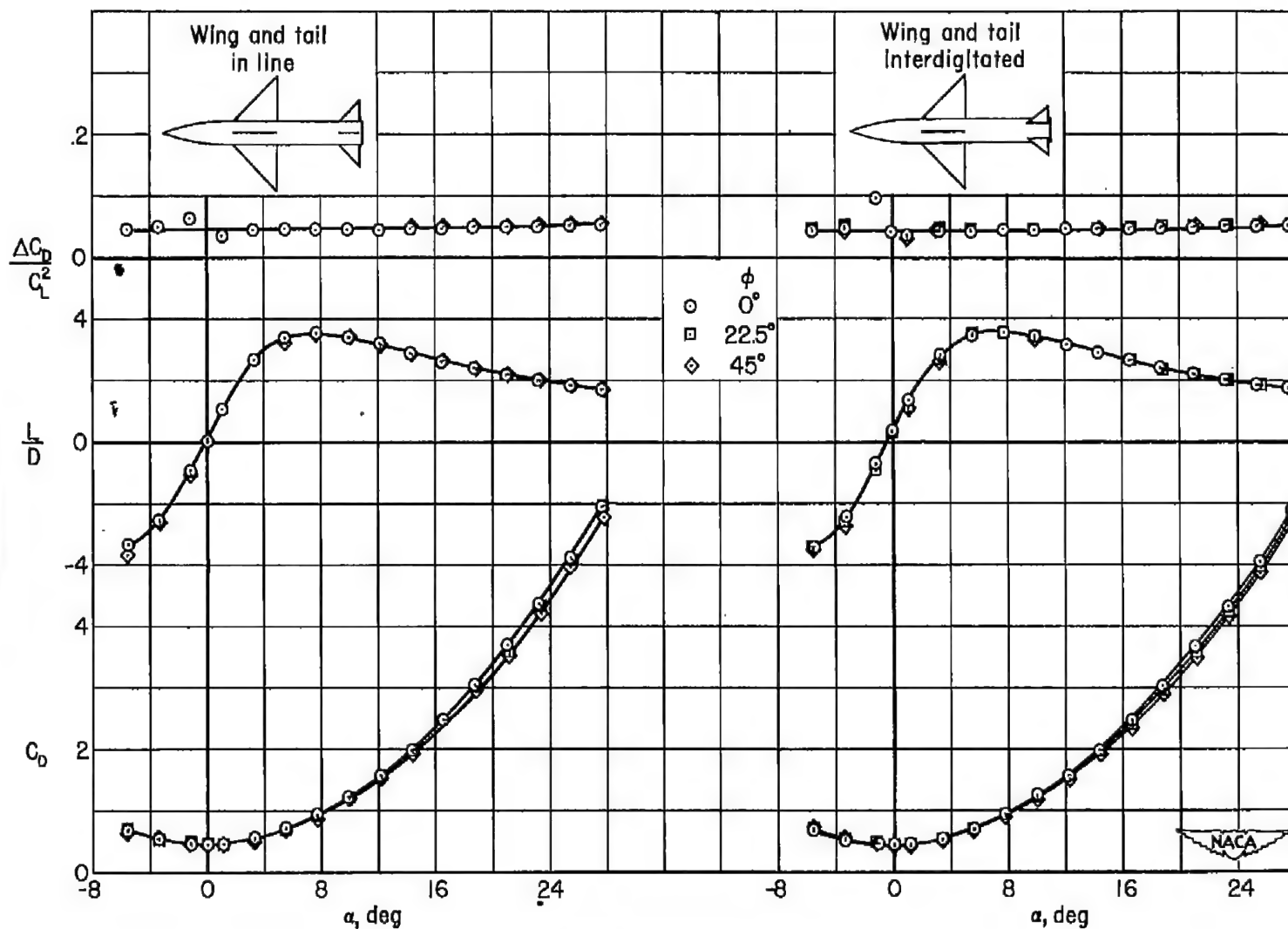
A-14139.1

Figure 3.- Strain-gage balance system.



(a) Lift and moment characteristics.

Figure 4.- Longitudinal characteristics of the body-wing-tail combination;  $\delta = 0^\circ$ .



(b) Drag characteristics.

Figure 4.- Concluded.



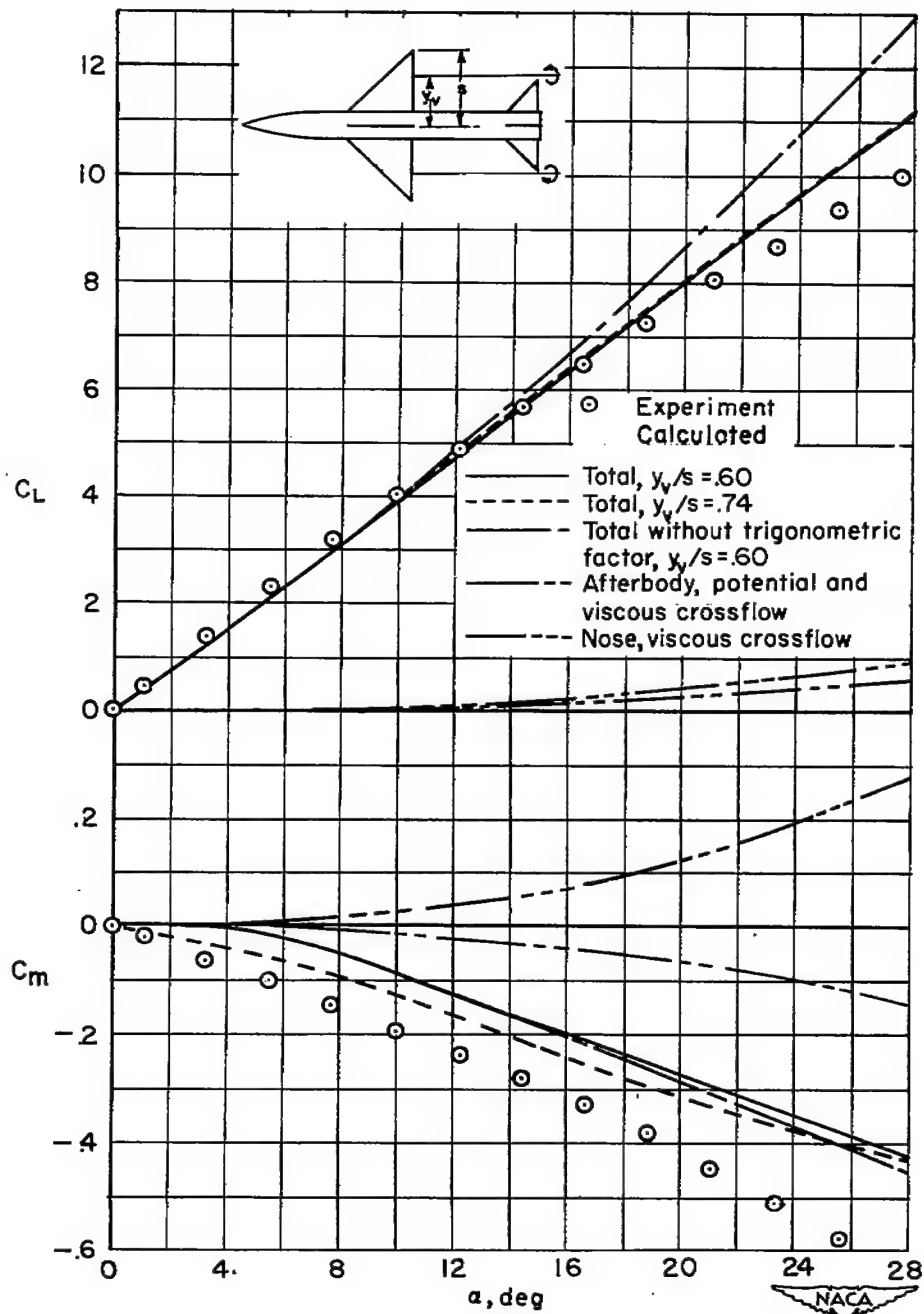
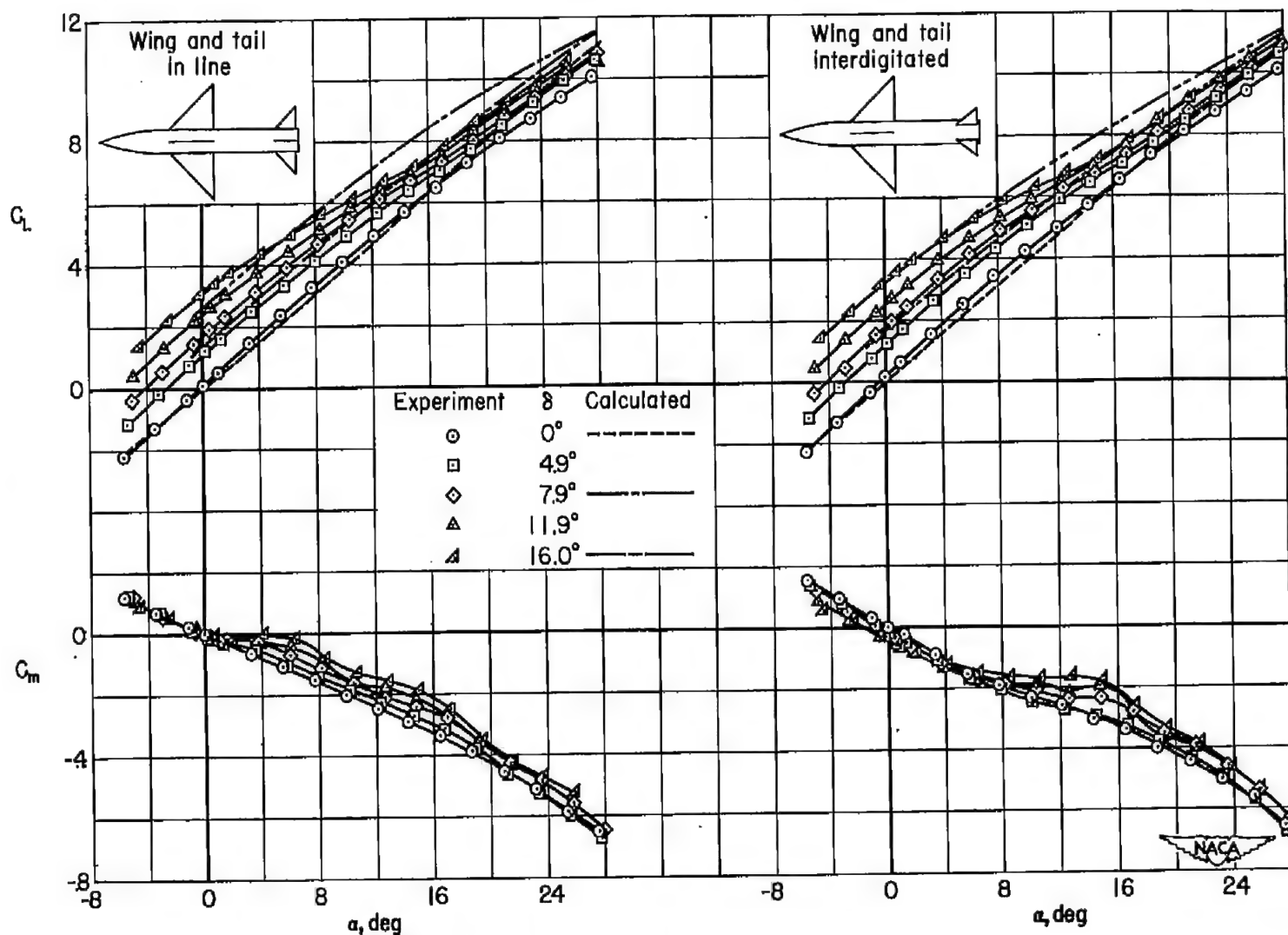
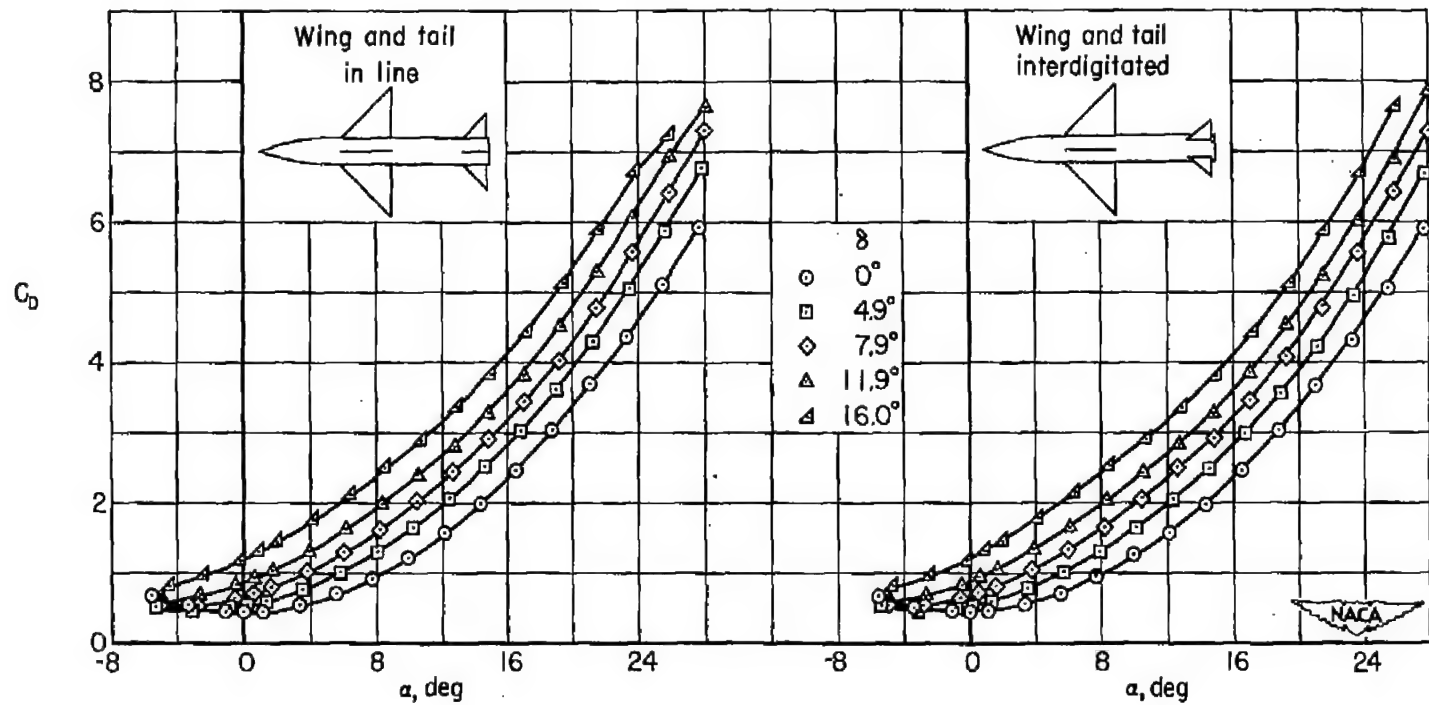


Figure 5.- Estimated effects of vortex spacing and contributions of the forebody and afterbody crossflow to the lift and pitching-moment characteristics; wing and tail inline,  $\phi = 0^\circ$ .



(a) Lift and moment characteristics.

Figure 6.- Wing control characteristics of the body-wing-tail combination;  $\phi = 0^\circ$ .



(b) Drag characteristics.

Figure 6.- Concluded.

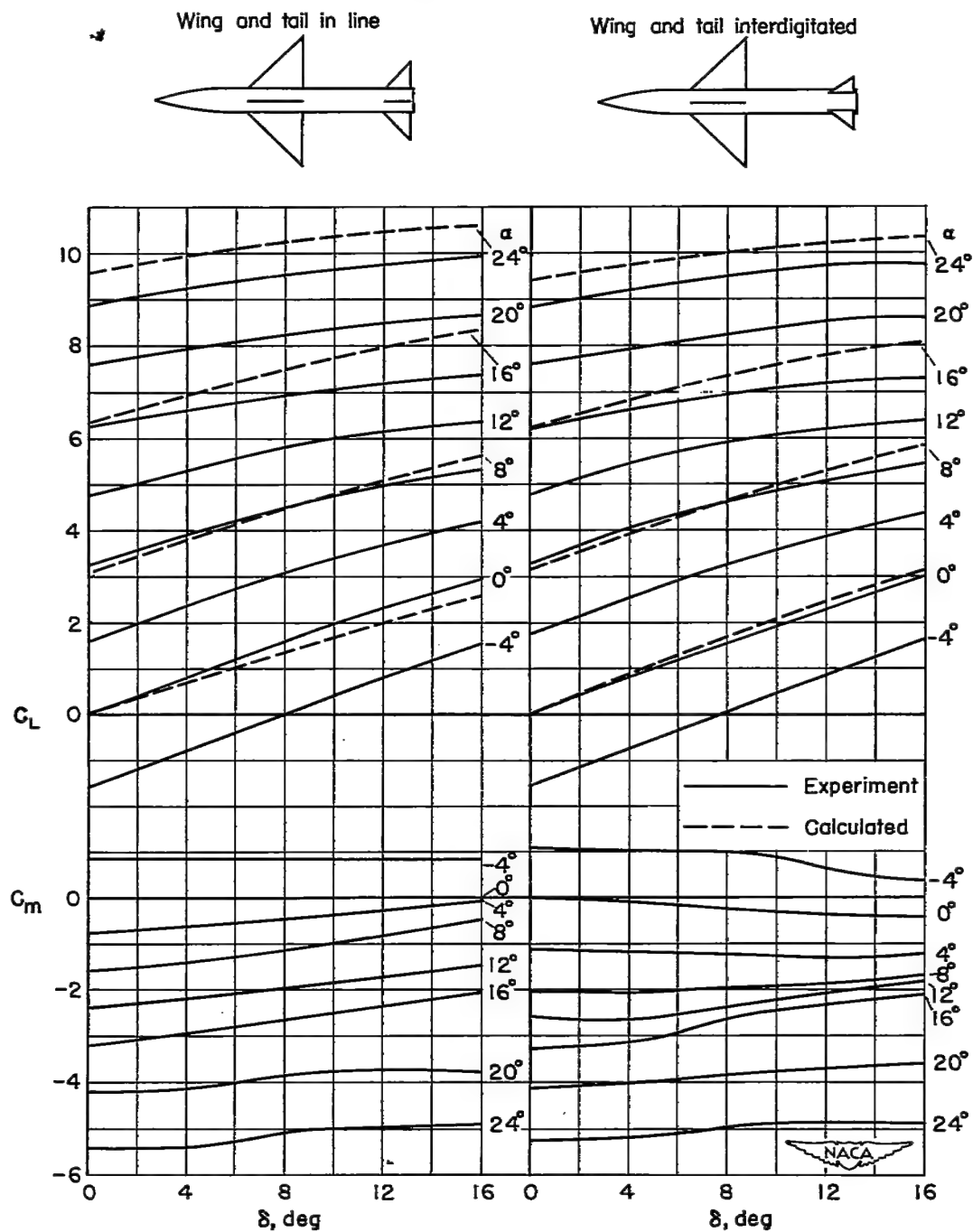
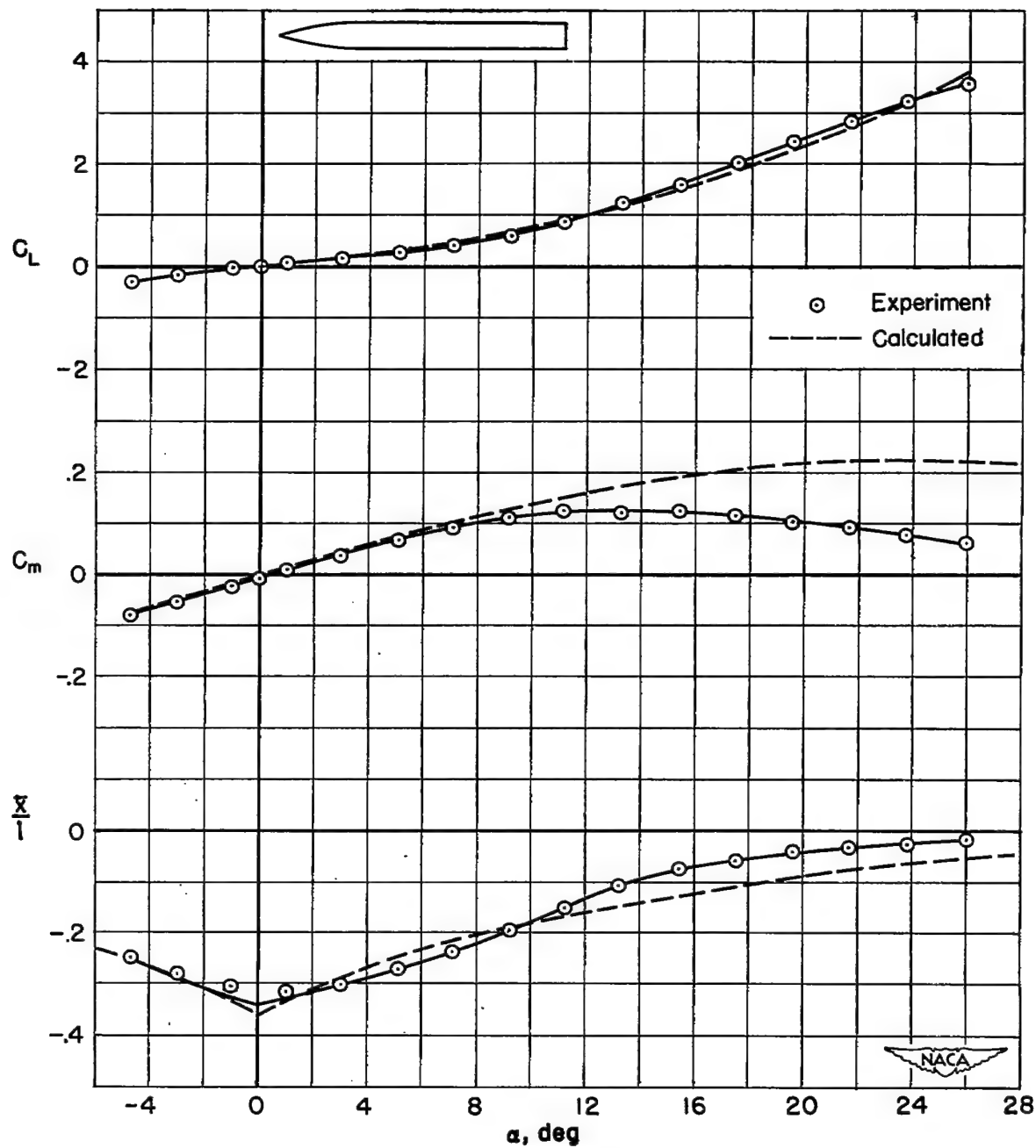
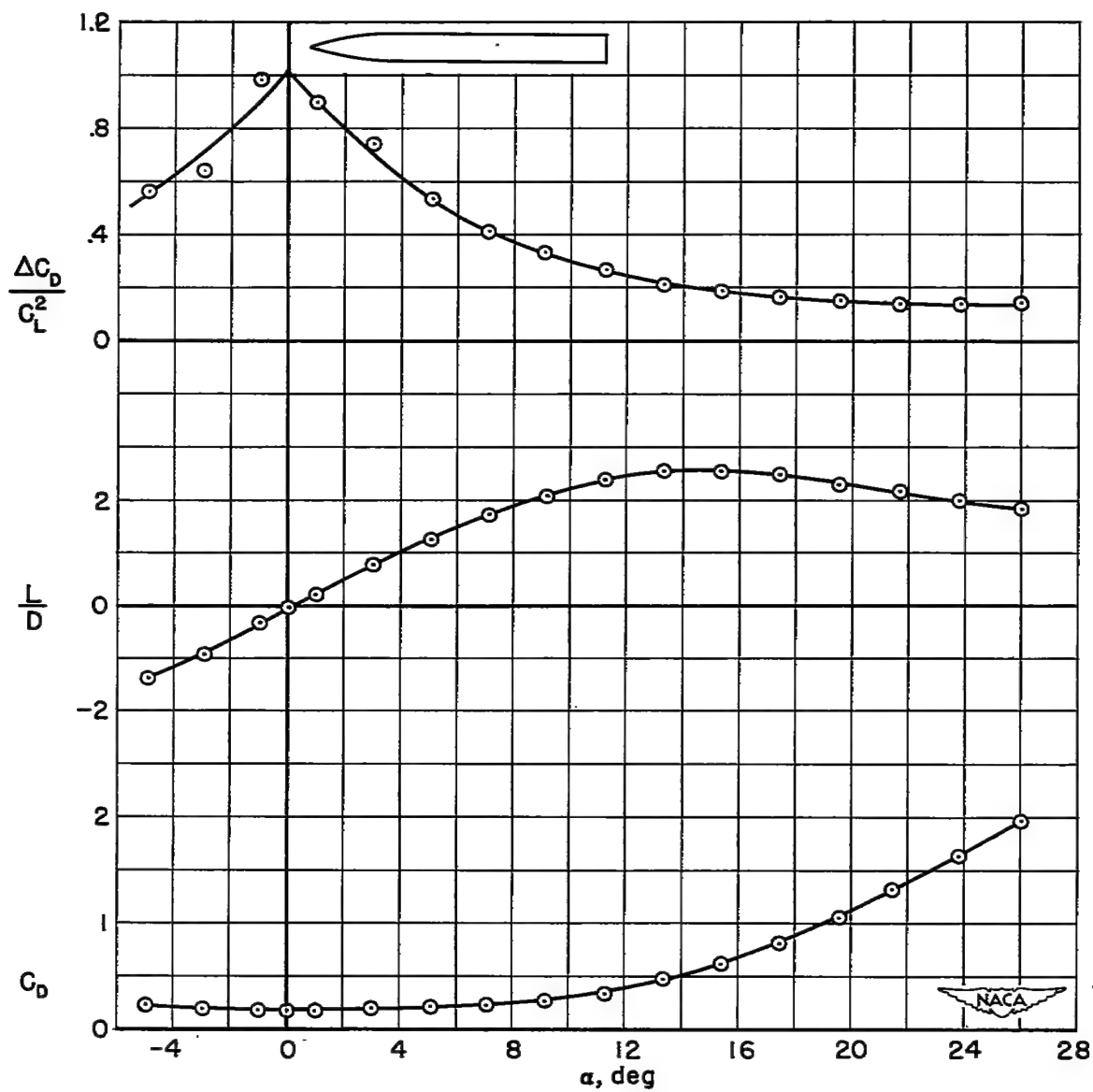


Figure 7.- Wing control effectiveness of the body-wing-tail combination;  
 $\varphi = 0^\circ$ .



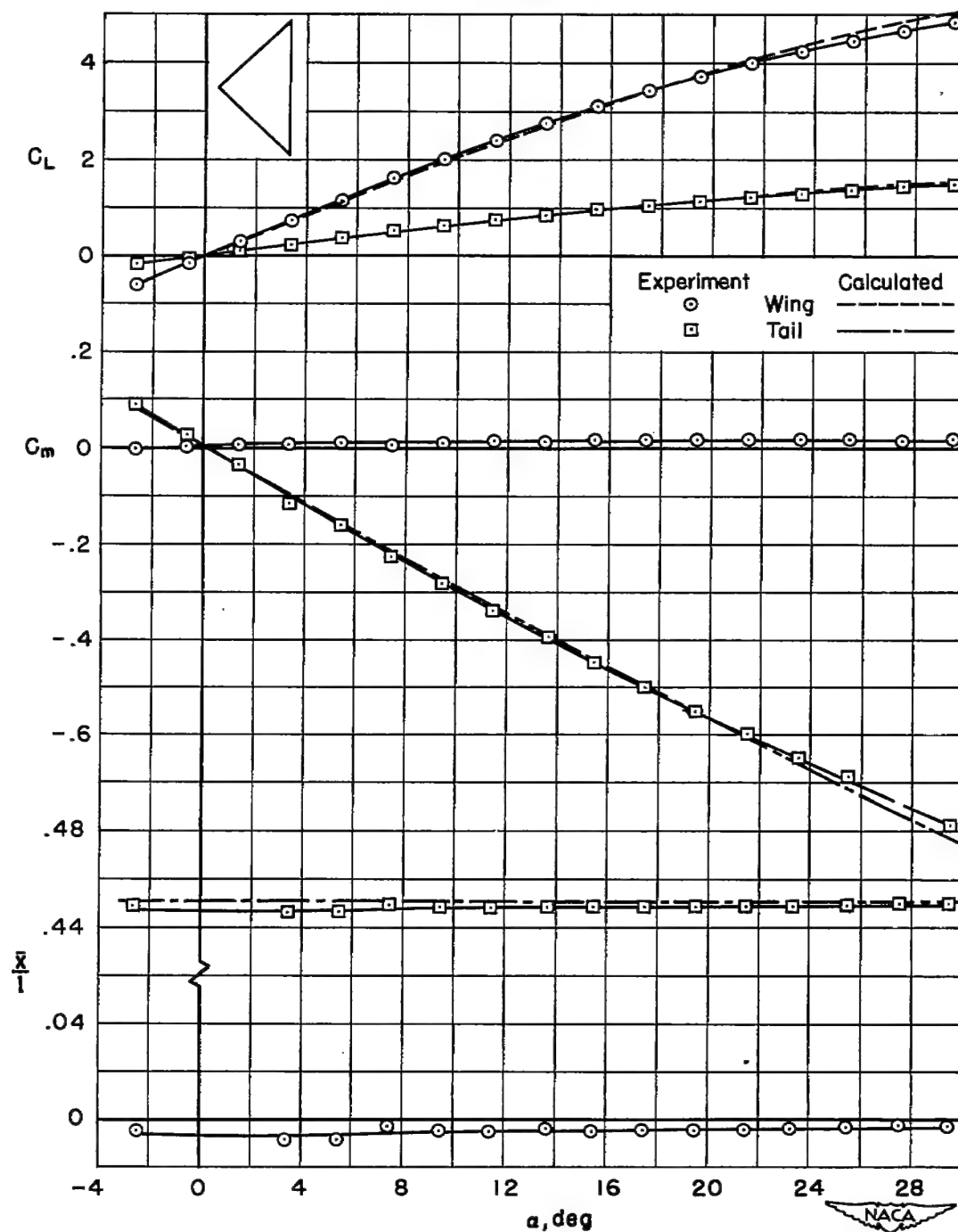
(a) Lift and moment characteristics.

Figure 8.- Longitudinal characteristics of the body.



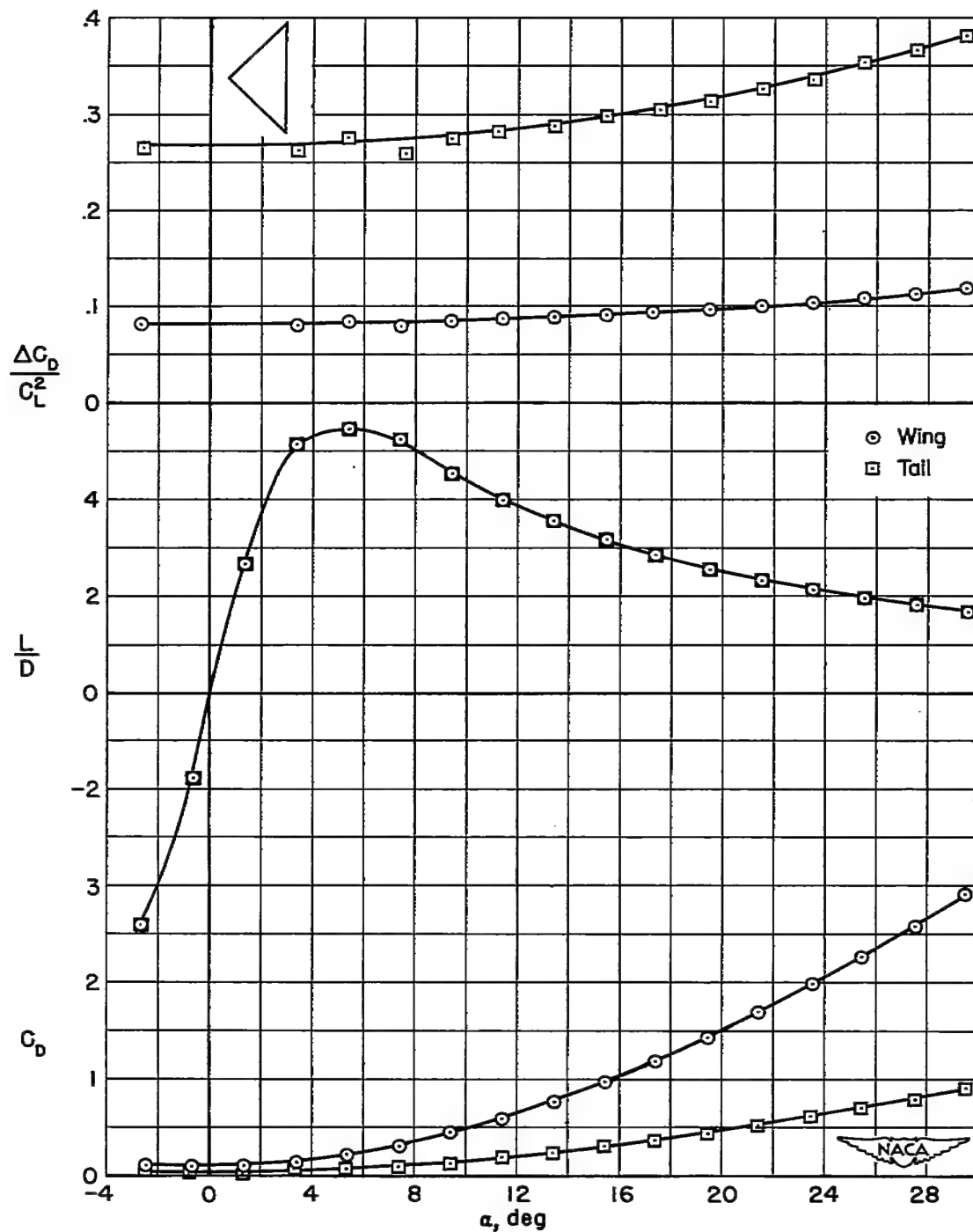
(b) Drag characteristics.

Figure 8.- Concluded.



(a) Lift and moment characteristics.

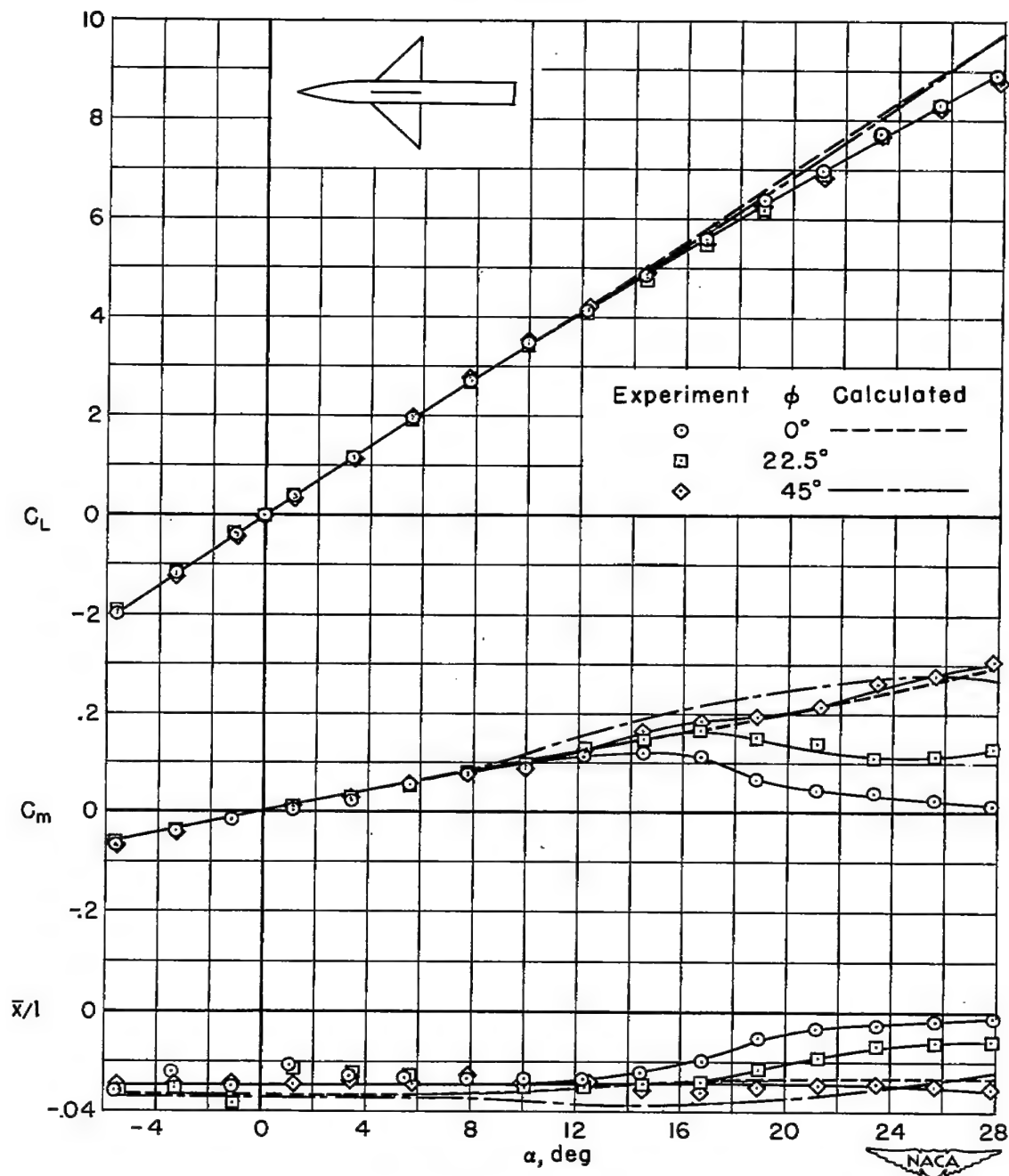
Figure 9.- Longitudinal characteristics of the wing and of the tail, based on the body area and length;  $\varphi = 0^\circ$ .



(b) Drag characteristics.

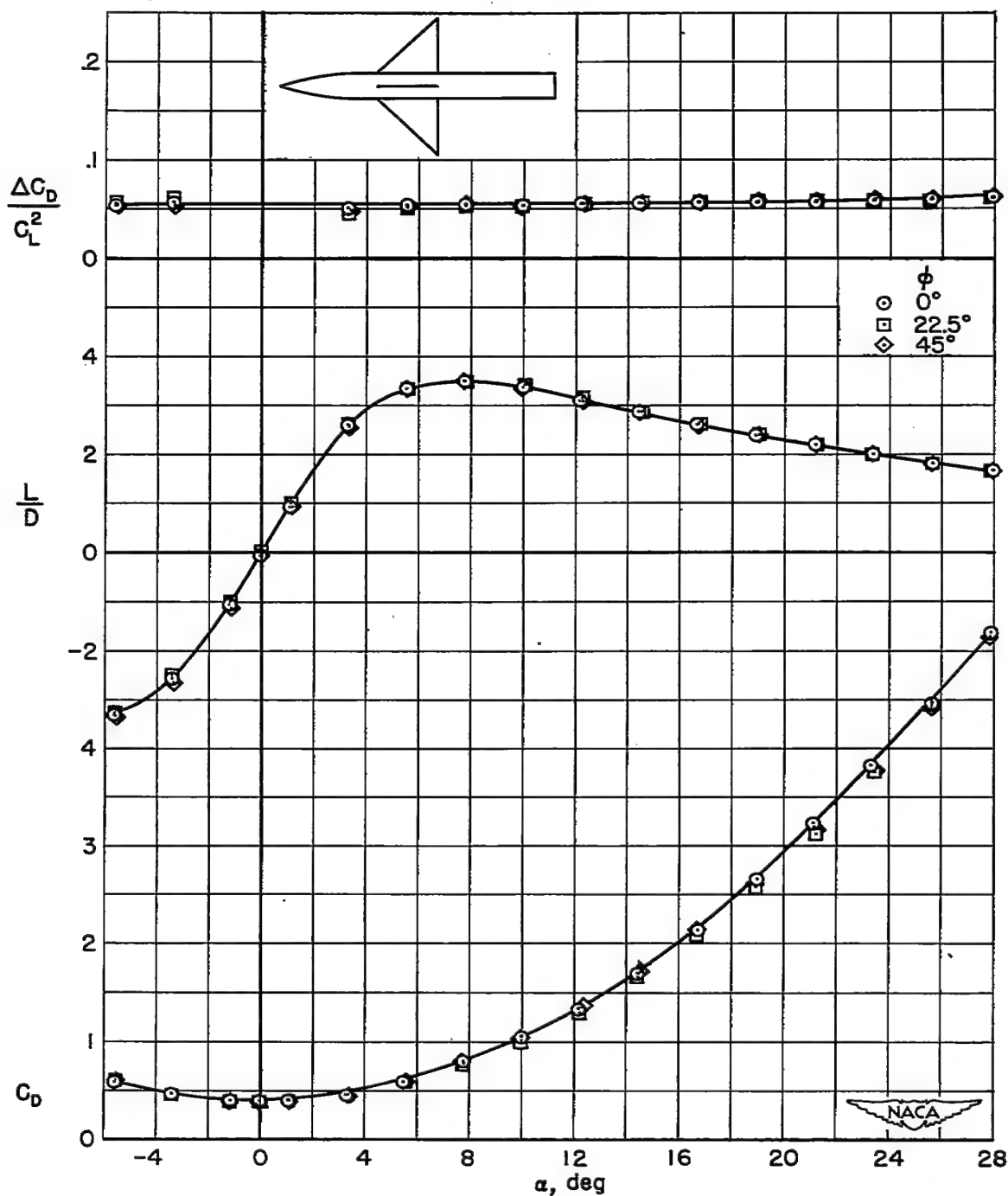
Figure 9.- Concluded.





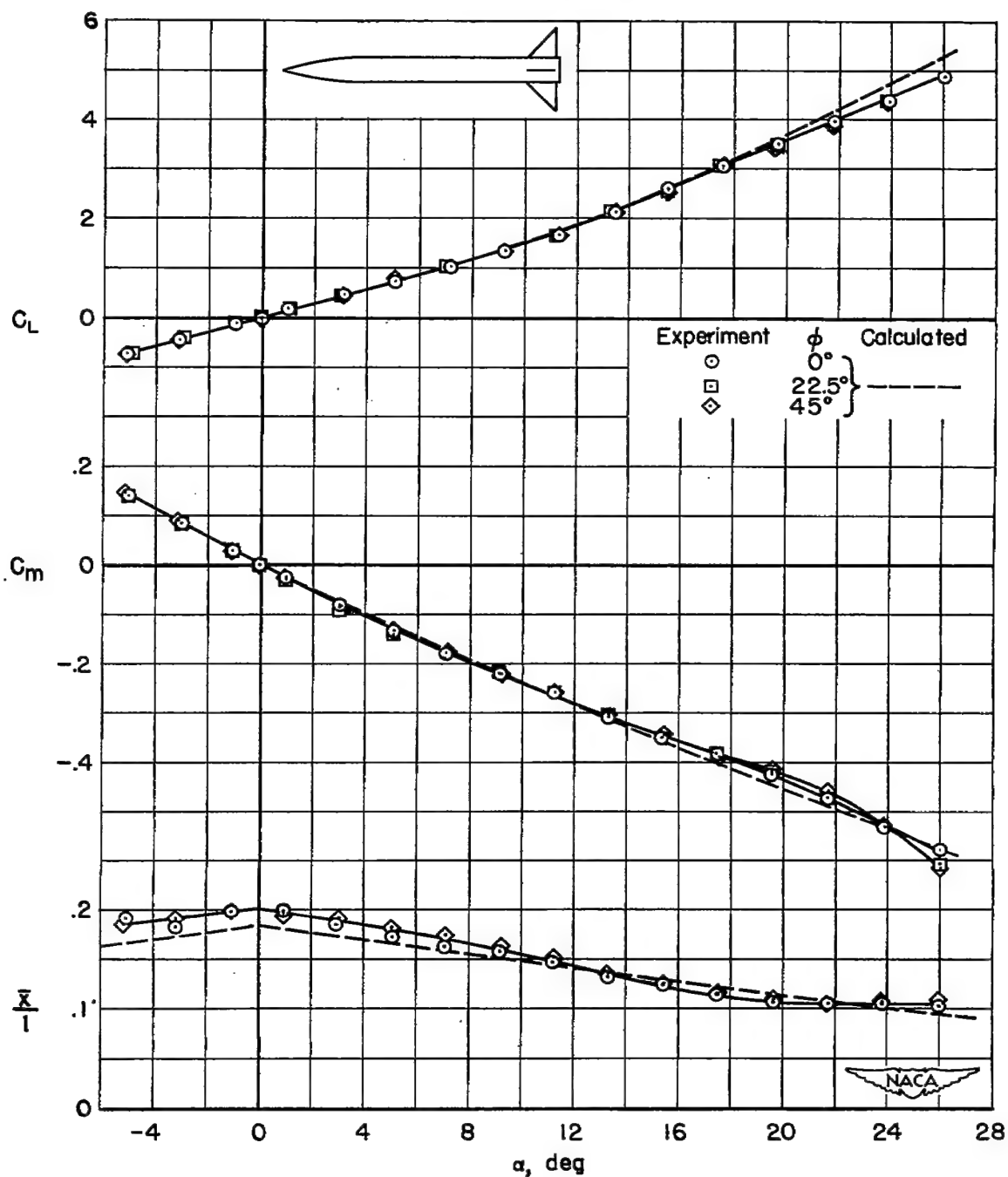
(a) Lift and moment characteristics.

Figure 10.- Longitudinal characteristics of the body-wing combination;  
 $\delta = 0^\circ$ .



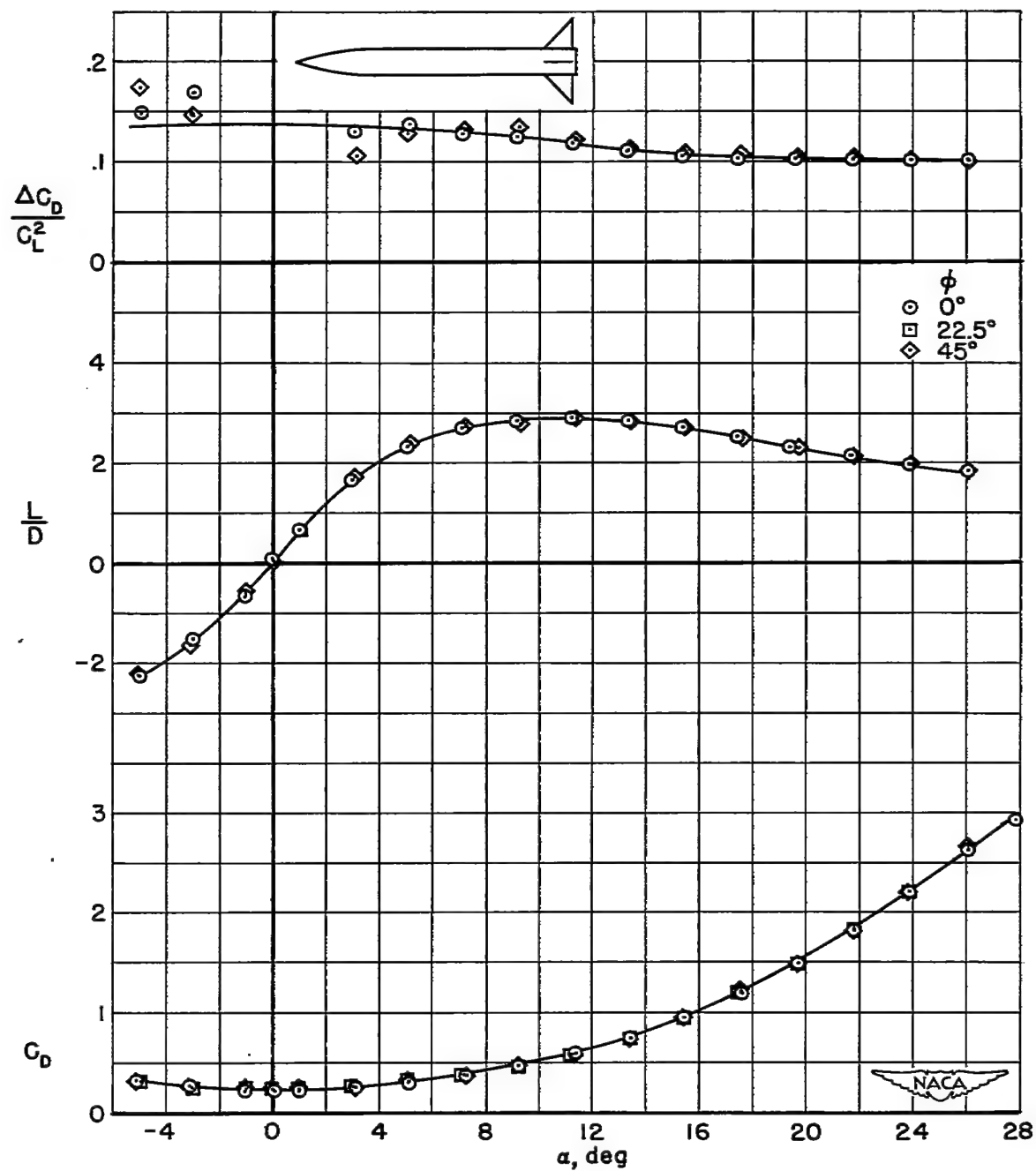
(b) Drag characteristics.

Figure 10.- Concluded



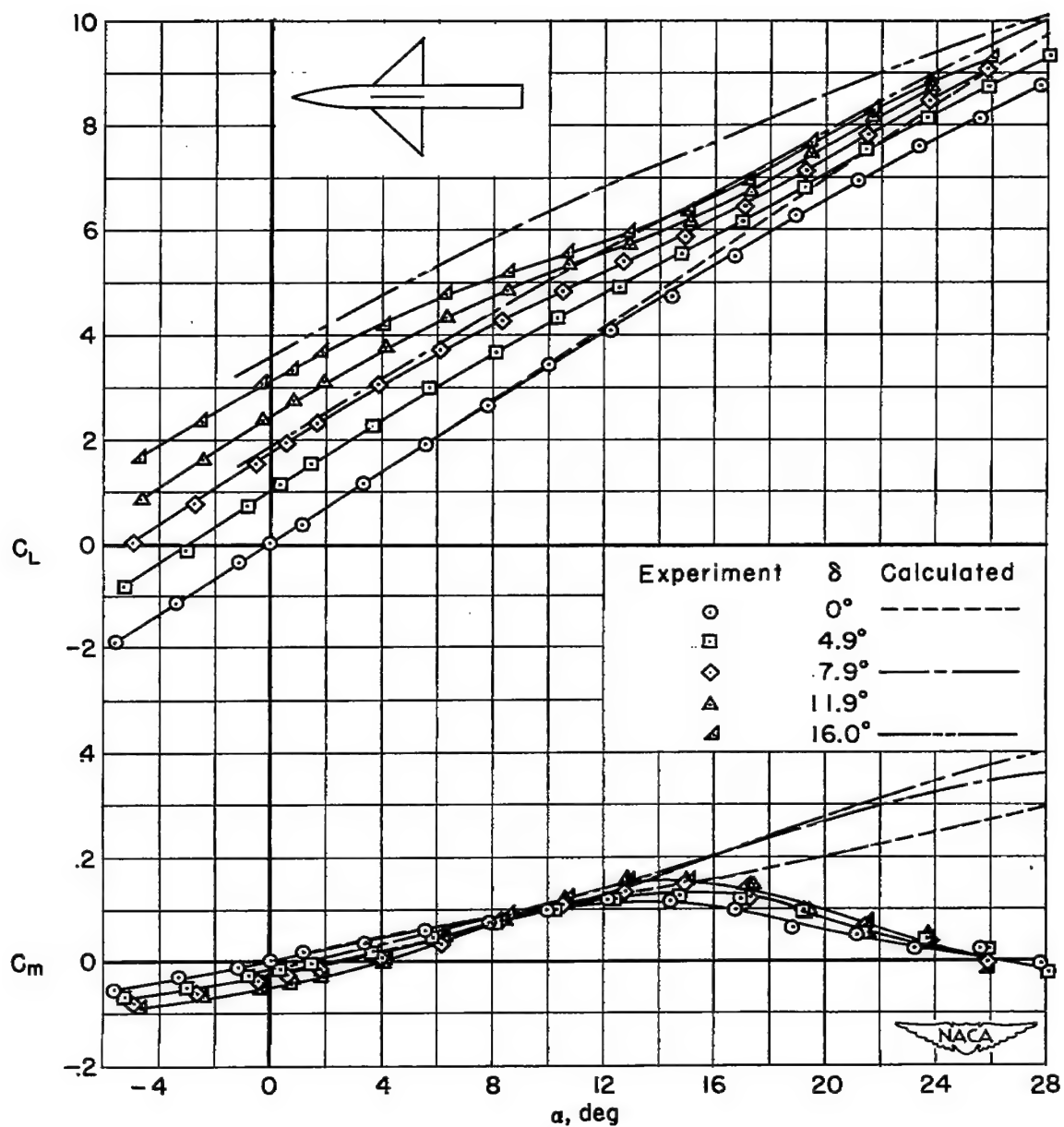
(a) Lift and moment characteristics.

Figure 11.- Longitudinal characteristics of the body-tail combination.



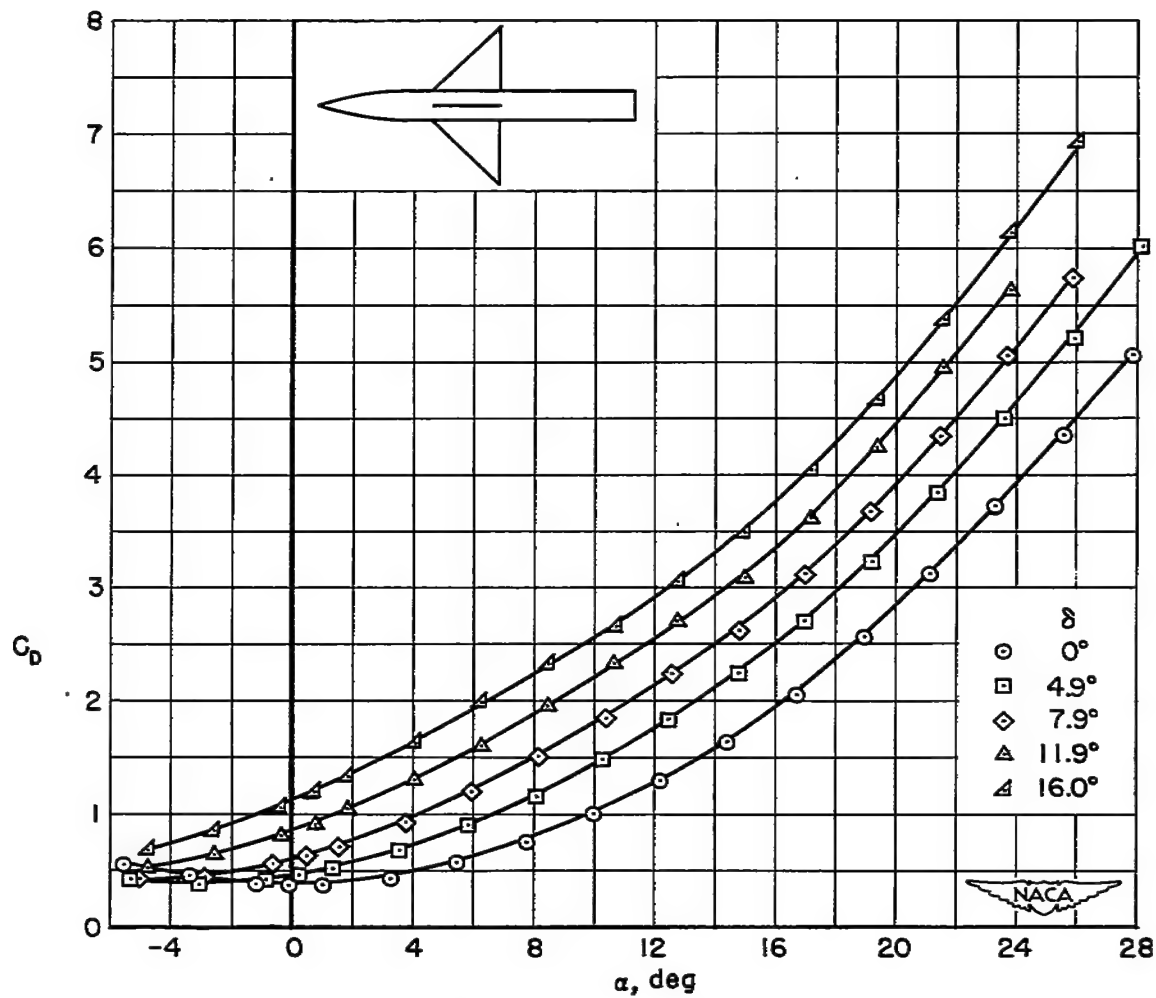
(b) Drag characteristics.

Figure 11.- Concluded



(a) Lift and moment characteristics.

Figure 12.- Wing control characteristics of the body-wing combination;  
 $\phi = 0^\circ$ .



(b) Drag characteristics.

Figure 12.- Concluded.

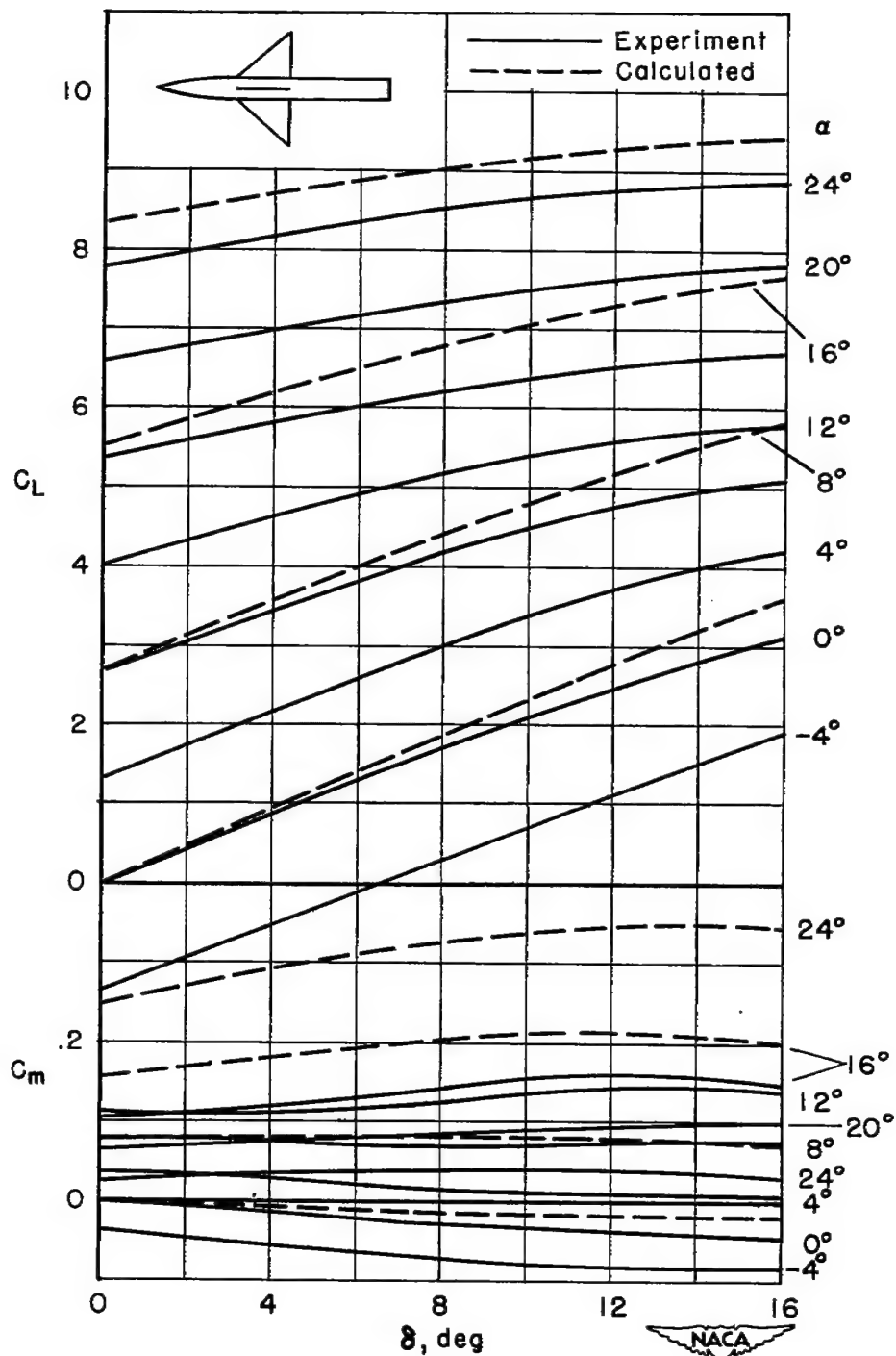


Figure 13.- Wing control effectiveness of the body-wing combination;  
 $\varphi = 0^\circ$ .

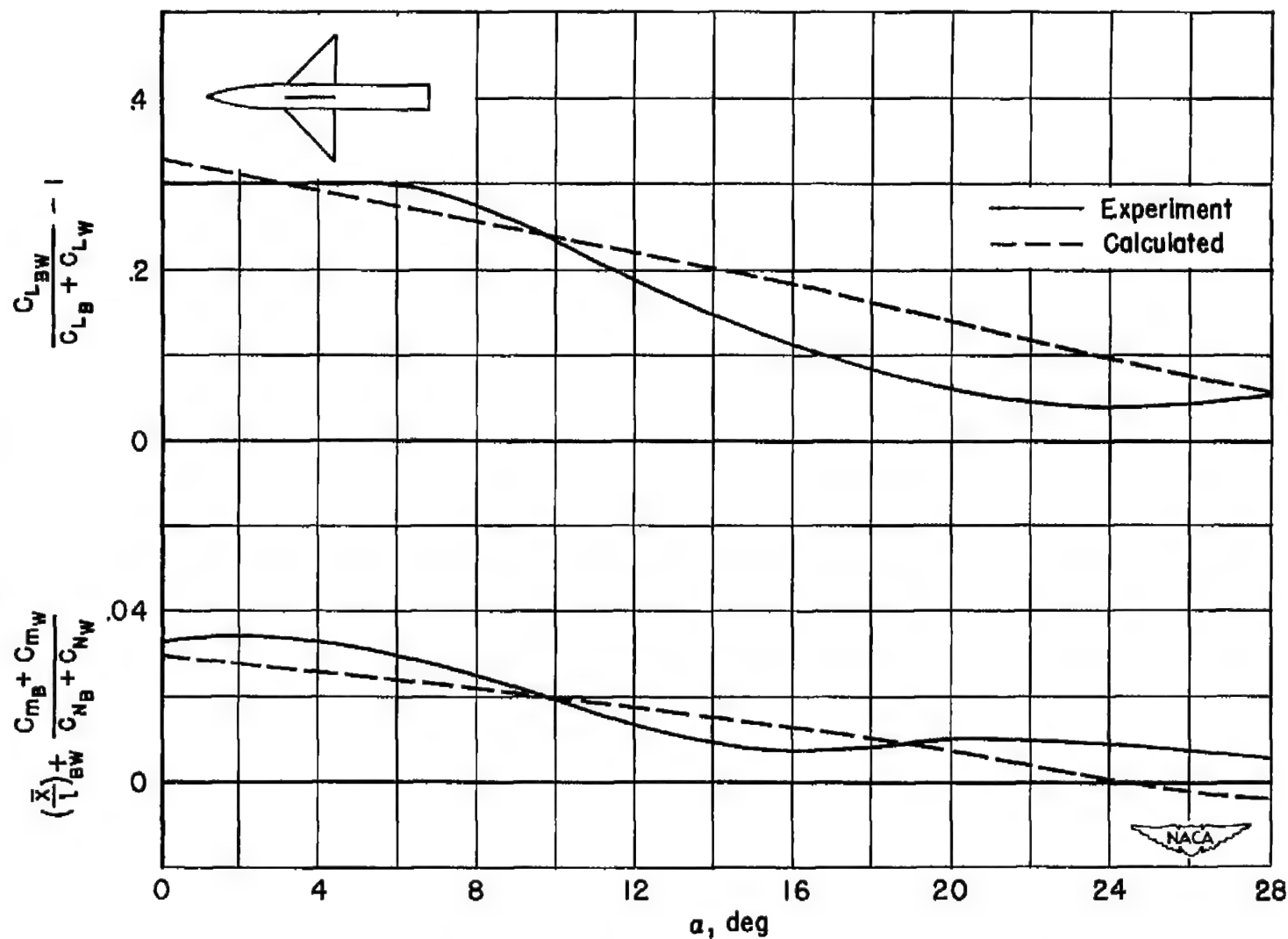


Figure 14.- Lift and moment interference characteristics of the body-wing combination;  $\delta = 0^\circ$ ,  $\phi = 0^\circ$ .



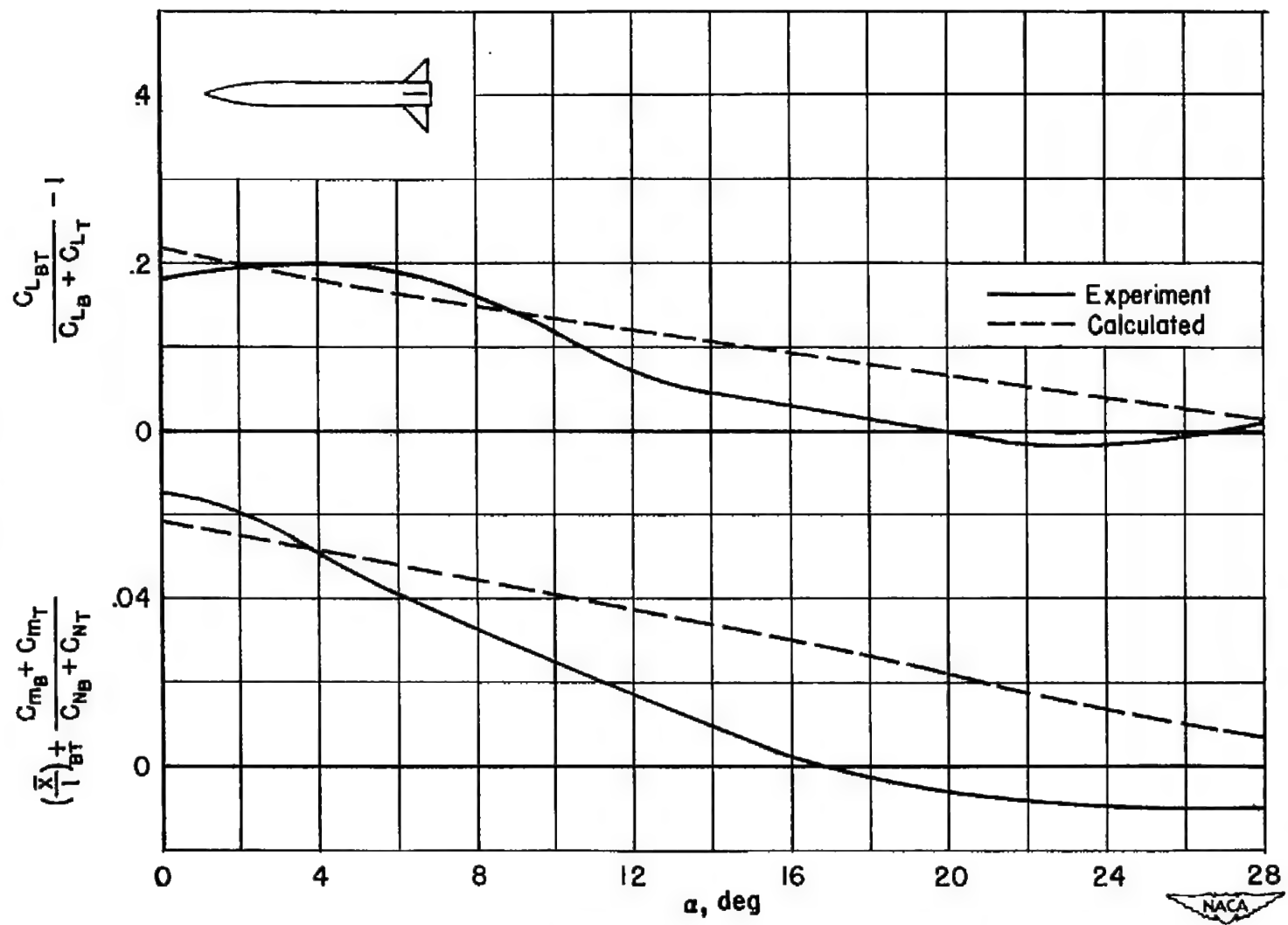


Figure 15.- Lift and moment interference characteristics of the body-tail combination;  $\phi = 0^\circ$ .

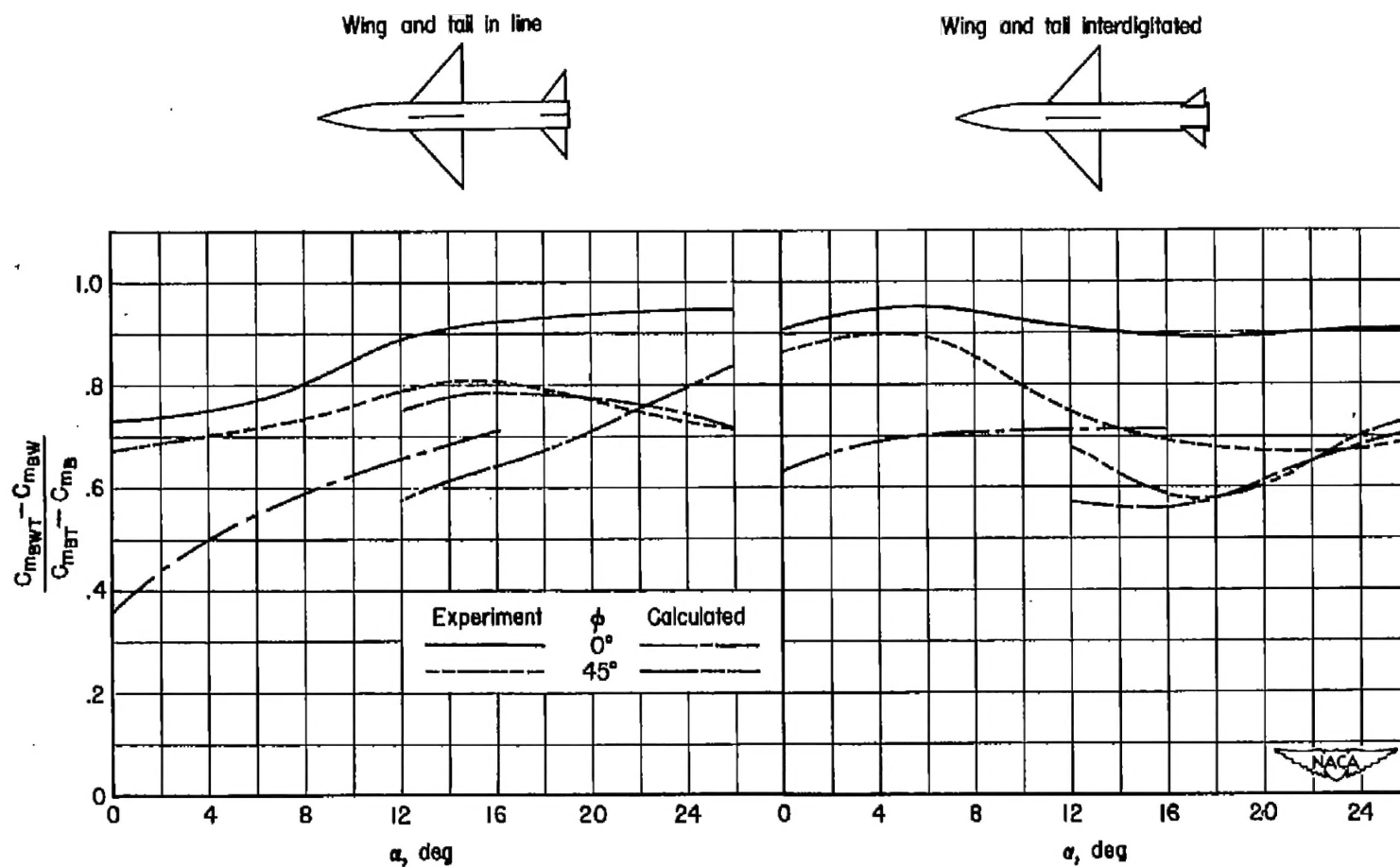
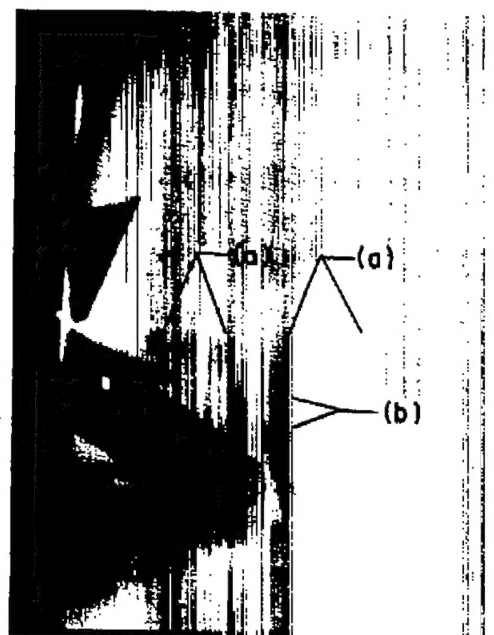
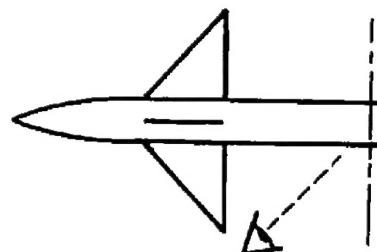
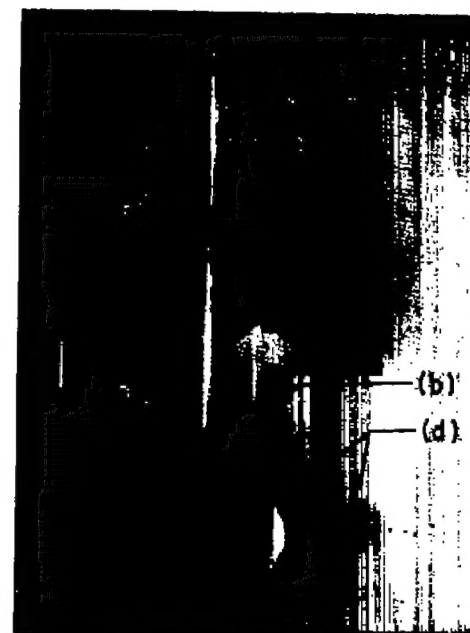


Figure 16.- Wing-tail interference characteristics of the body-wing-tail combination;  $\delta = 0^\circ$ .

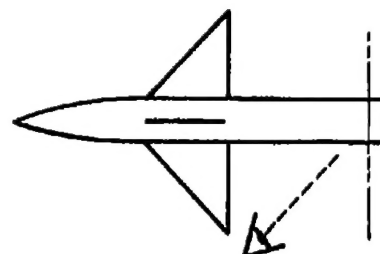
- (a) Wing vortices
- (b) Body vortices
- (c) Vortices from upper wing panels
- (d) Vortices from lower wing panels


 $\phi = 0^\circ$ 

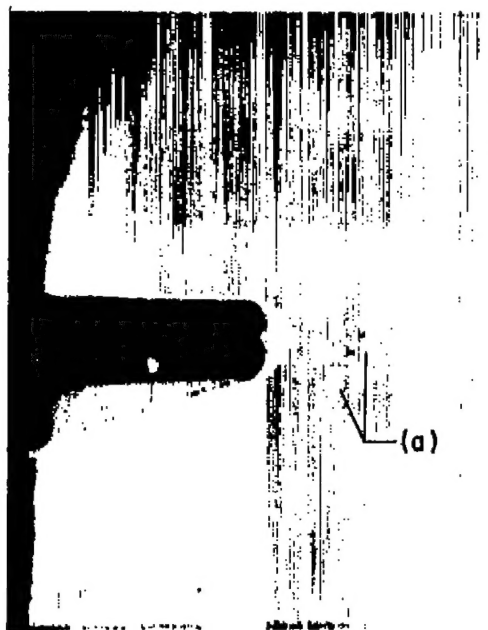
 $\phi = 22.5^\circ$ 

 $\phi = 45^\circ$ 

A-19354.1

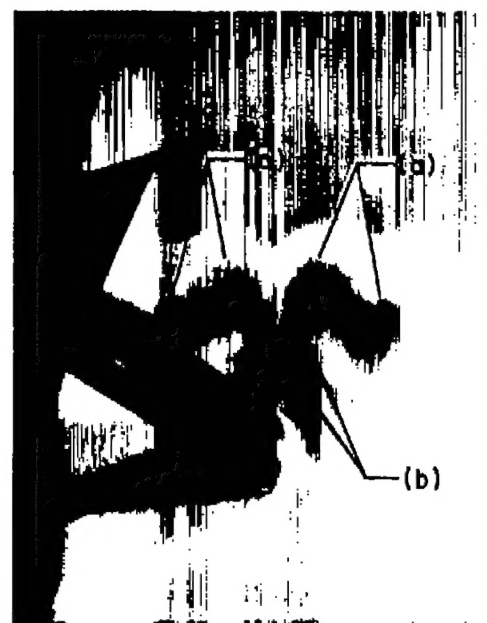
Figure 17.- Vapor-screen photographs of the vortex wake at tail location of the body-wing combination;  $\alpha = 27.8^\circ$ ,  $\delta = 0^\circ$ .



(a) Wing vortices  
(b) Body vortices



$\phi = 0^\circ$



$\phi = 28.2^\circ$

A-19355.1

Figure 18.- Vapor-screen photographs of the vortex wake at tail location of the body-wing combination;  $\delta = 16.0^\circ$ ,  $\phi = 0^\circ$ .

UNCLASSIFIED



3 1176 01434 7729

UNCLASSIFIED